Heidari Hafshejani et al., *BioImpacts*. 2026;16:33538
doi:10.34172/bi.33538
https://bi.tbzmed.ac.ir

Design and evaluation of a multifunctional electrospun scaffold loaded with amniotic membrane and allantoin for dermal tissue engineering

Nahid Heidari Hafshejani[1], Azam Rahimpour[1], Hojjat Allah Abbaszadeh[2,3], Hojatollah Montazeri[4], Sepideh Ghani[5], Simzar Hosseinzadeh[4,6*], Bahram Kazemi[1,5,7*]

[1]Department of Medical Biotechnology, School of Advanced Technologies in Medicine, Shahid Beheshti University of Medical Sciences, Tehran, Iran
[2]Laser Applications in Medical Sciences Research Center, Shahid Beheshti University of Medical Sciences, Tehran, Iran
[3]Hearing Disorders Research Center, Loghman Hakim Hospital, Shahid Beheshti University of Medical Sciences, Tehran, Iran
[4]Department of Tissue Engineering and Applied Cell Sciences, School of Advanced Technologies in Medicine, Shahid Beheshti University of Medical Sciences, Tehran, Iran
[5]Cellular and Molecular Biology Research Center, Shahid Beheshti University of Medical Sciences, Tehran, Iran
[6]Medical Nanotechnology and Tissue Engineering Research Center, Shahid Beheshti University of Medical Sciences, Tehran, Iran
[7]Parasitology Department, School of Medicine, Shahid Beheshti University of Medical Sciences, Tehran, Iran

Article Info



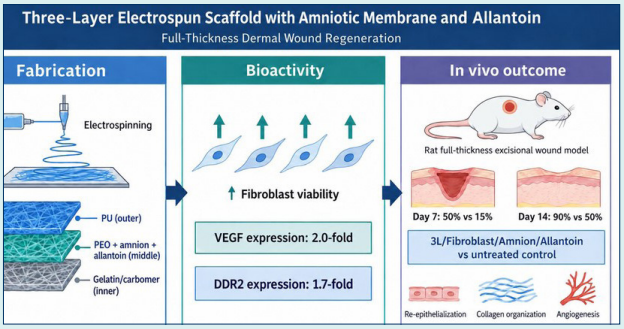
Article Type:
Original Article

Article History:
Received: 10 Feb. 2026
Revised: 14 Sep. 2026
Accepted: 16 Sep. 2026
ePublished: 11 Nov. 2026

Keywords:
Electrospun scaffold
Skin tissue
Nanofibers
Allantoin
Amniotic membrane powder
Tissue engineering

Abstract

Introduction: Chronic wounds remain difficult to treat because healing is impaired, inflammation persists, and infection risk is high. Whether a spatially organized three-layer electrospun scaffold containing amniotic membrane powder and allantoin can combine mechanical support with sustained bioactive delivery during full-thickness dermal regeneration remains unclear.



Methods: The scaffold was electrospun in 3 layers: polyurethane, polyethylene oxide containing amniotic membrane powder and allantoin, and a gelatin/carbomer blend. Physicochemical properties and fibroblast responses were assessed, followed by wound healing in a rat full-thickness excisional model (n = 12 per group; n = 3 per time point) over 21 days.

Results: All layers displayed uniform nanofibers. The 3L/Amnion/Allantoin scaffold reached an ultimate tensile strength of 38.19 MPa. Superhydrophilic behavior, with a contact angle of 0°, was observed for 3L/Allantoin. The 3L/Amnion/Allantoin scaffold increased fibroblast viability ($P < 0.0001$ versus controls at day 14) and upregulated VEGF (2-fold) and DDR2 (1.7-fold) expression. On day 7, wound closure reached 50.0 ± 1.0% in the 3L/Fibroblast/Amnion/Allantoin group versus 15.0 ± 1.0% in the untreated control ($P < 0.0001$). By day 14, this group reached 90.0 ± 1.0% closure versus 50.0 ± 1.0% in controls ($P < 0.0001$), accompanied by accelerated re-epithelialization and organized collagen deposition. By day 21, wound closure reached ≥ 99% in all groups, with no significant intergroup differences.

Conclusion: The three-layer scaffold combined structural reinforcement with local bioactive delivery and accelerated wound closure through day 14, supporting further evaluation in dermal tissue engineering.

Introduction

Skin functions as the body's primary barrier, protecting underlying tissues from microbial invasion, mechanical damage, and dehydration.[1] In a normal physiological state, wound healing proceeds through a highly regulated sequence of hemostasis, inflammation, proliferation, and

*Corresponding authors: Simzar Hosseinzadeh, Email: s.hosseinzadeh@sbmu.ac.ir, Bahram Kazemi, Email: bahram_14@yahoo.com

© 2026 The Author(s). This work is published by BioImpacts as an open access article distributed under the terms of the Creative Commons Attribution Non-Commercial License (http://creativecommons.org/licenses/by-nc/4.0/). Non-commercial uses of the work are permitted, provided the original work is properly cited.

extracellular matrix (ECM) remodeling.[2] In contrast, minor injuries usually repair without these complications, and full-thickness wounds often have delayed recovery accompanied by significant clinical and economic challenges. To overcome these issues, wound scaffolds play a vital role in promoting dermal repair.[3] An ideal wound scaffold should support tissue integrity while promoting a balanced wound microenvironment conducive to healing. Key requirements include effective exudate management, antimicrobial protection, moisture and temperature regulation, and cytocompatibility to support fibroblast proliferation. Additionally, such scaffolds should minimize inflammatory or allergic responses and remain economically feasible for clinical application, particularly in the management of chronic wounds.[4-7] Despite significant advances in wound care technologies, the integration of these functions within a single network remains a major challenge. Most conventional materials cannot address all essential aspects of dermal wound healing. This limitation suggests that advanced biomaterials should be designed to meet the therapeutic requirements of dermal tissue. Recent advances in wound scaffolds have increasingly focused on the architecture of dermal scaffolds to replicate the structural and biological properties of native skin ECM. In this manner, nanofibrous scaffolds have attracted attention for their ability to promote cell adhesion, migration, and proliferation while facilitating gas exchange and nutrient transport.[8,9] Electrospinning has emerged as a promising technique for wound scaffold fabrication due to its ability to produce fibrous structures that closely mimic the native ECM. Electrospun nanofibrous scaffolds offer high surface area, interconnected porosity, and enhanced cell–material interactions, making them particularly suitable for skin regeneration.[9,10] Recent studies have further highlighted the potential of electrospun wound dressings by demonstrating their ability to combine structural support, controlled bioactive delivery, and modulation of the wound microenvironment within a single platform, making them promising candidates for the treatment of chronic and hard-to-heal wounds.[11]

To effectively address the multifactorial requirements of wound healing, recent strategies have shifted toward multilayer and functionally graded wound scaffolds, in which each layer is designed to perform a distinct biological or physicochemical function. Such architectures enable the simultaneous integration of barrier protection, bioactive delivery, and moisture regulation within a single membrane system, addressing limitations associated with monofunctional scaffolds.[12] Recent advances in multifunctional electrospun dressings have also emphasized the importance of integrating regenerative cues with antimicrobial and angiogenic properties to accelerate tissue repair and enhance healing outcomes.[13]

Despite advances in electrospun wound dressings, most multilayer scaffolds incorporate single bioactive agents or conventional polymer combinations.[14-16] The simultaneous integration of amniotic membrane powder and allantoin within a spatially organized tri-layer electrospun scaffold composed of polyurethane, polyethylene oxide, and carbomer/gelatin has not been previously reported.

In this context, a three-layer nanofibrous scaffold was designed to reproduce the hierarchical structure of native skin while preserving its functionality. The outer layer served as a protective barrier, the intermediate layer acted as a reservoir for allantoin and amniotic membrane powder, and the inner layer maintained a moist interface with the wound. Polyurethane (PU) was selected as the outer layer due to its favorable mechanical stability for skin tissues. PU is a polymer that provides a balance of flexibility and mechanical strength, essential for dermal wounds in a dynamic, mobile environment. Moreover, PU exhibits appropriate oxygen permeability and water vapor transmission, making it suitable for skin applications.[17-22] The intermediate layer was fabricated using polyethylene oxide (PEO) as a hydrophilic carrier matrix to host the bioactive agents amniotic membrane powder and allantoin, aiming to improve wound healing by providing a moist microenvironment and facilitating sustained local delivery.[23-25] PEO is a hydrophilic and biodegradable polymer widely used in electrospun drug delivery systems due to its excellent biocompatibility and ability to form uniform nanofibers, enabling effective incorporation and controlled release of bioactive agents.[26] Allantoin is a wound-healing agent that modulates tissue repair by enhancing fibroblast activity, promoting granulation tissue formation, and modulating inflammatory responses, ultimately supporting tissue repair.[27] Multiple underlying mechanisms mediate allantoin's wound-healing properties. Allantoin facilitates wound healing by regulating the inflammatory response, reducing the infiltration of inflammatory cells into the wound site, and stimulating fibroblast proliferation and extracellular matrix synthesis. Additionally, allantoin promotes early collagen deposition, which is crucial for granulation tissue formation and tissue remodeling.[27, 28] Its keratolytic and antimicrobial actions, along with the previously noted features, make allantoin particularly beneficial for wound healing.[29]

Similarly, the native human amniotic membrane contains extracellular matrix proteins and bioactive factors associated with reduced inflammation, epithelial repair, and protection against infection. Incorporation of allantoin and amniotic membrane powder into the PEO matrix is expected to facilitate uniform distribution and sustained local availability of bioactive agents at the wound site.[30-32] Recent electrospun nanofiber systems incorporating bioactive components have demonstrated enhanced wound regeneration through improved cell–material interactions, moisture retention, and stimulation of tissue remodeling processes.[33]

The inner layer was composed of a carbomer/gelatin blend, selected for its hydrophilicity and biocompatibility to promote moisture retention and ensure intimate contact with the wound surface. Gelatin is a collagen-

derived component that provides cell-adhesion sites through its Arg-Gly-Asp (RGD) sequences, thereby supporting cellular proliferation and migration.[34] Gelatin-based scaffolds also demonstrate good biocompatibility and biodegradability and have been widely used in wound-scaffold applications due to their ability to mimic the natural ECM.[35] Others have reported that during the healing process, electrospun membranes containing gelatin promote better cell attachment and spreading due to their resemblance to native skin tissue.[36] Carbomer provides high viscosity and bioadhesive properties in polymeric matrices,[37] and carbomer-based systems have shown good biocompatibility and sustained release of bioactive molecules in wound models.[38, 39] Together, these properties enable prolonged retention of bioactive molecules at the wound site, thereby supporting an optimal environment for wound healing. Accordingly, this study focused on developing and evaluating a three-layer electrospun nanofibrous scaffold incorporating spatially organized functional components to meet the complex demands of wound healing.

Materials

Polyurethane (PU), polyethylene oxide (PEO), gelatin, Carbomer, allantoin, tetrahydrofuran (THF), N, N-dimethylformamide (DMF), glacial acetic acid (40%), amniotic membrane powder, 3-(4,5-dimethylthiazol-2-yl)-2,5-diphenyltetrazolium bromide (MTT) powder, and dimethyl sulfoxide (DMSO) were purchased from Sigma-Aldrich (St. Louis, MO, USA). Fetal bovine serum (FBS) was purchased from Gibco (Thermo Fisher Scientific, USA). Dulbecco's Modified Eagle Medium, penicillin/streptomycin, and trypsin–EDTA solution were obtained from DNA Biotech Co. (Iran). An RNA extraction kit was provided by Gibco (Thermo Fisher Scientific, USA), and SYBR Green was obtained from Yekta Tajhiz (Tehran, Iran). Human fibroblast cells (Hu02) were obtained from the Pasteur Institute of Iran (Tehran, Iran). Adult male Wistar rats were supplied by the Laboratory Animal Center of Tehran University (Tehran, Iran).

Methods

Scaffold fabrication

The three-layer nanofibrous scaffold was prepared by electrospinning under controlled laboratory conditions (22 ± 1 °C and 40 ± 5% relative humidity). The electrospinning system consisted of a syringe pump, a high-voltage power supply, and a rotating drum collector lined with aluminum foil. All materials were purchased from commercial sources (Sigma-Aldrich, USA) and used as received without any further purification. All layers were fabricated sequentially under optimized parameters summarized in Table 1. For the first layer, a 12 wt% PU solution was prepared by dissolving 0.72 g PU in 6 mL of THF/DMF (3:1 v/v), and the mixture was stirred for 24 h at room temperature to obtain a homogeneous solution. The solution was electrospun using a 20-gauge needle at 14.5 kV, a flow rate of 0.2 mL/h, and a collector rotation speed of 300 rpm to form the PU base layer. For the second layer, a 12 wt% PEO solution was prepared by dissolving 0.72 g PEO in 6 mL deionized water. Amniotic membrane powder (1.5 wt%, corresponding to 0.09 g in 6 mL) and allantoin (0.75 wt%, corresponding to 0.045 g in 6 mL) were mixed to obtain a uniform suspension. These concentrations were chosen based on experimental experience and in accordance with previously reported studies, which showed that similar concentration ranges yield bead-free nanoscale morphology. The mixture was electrospun directly onto the PU layer, and control scaffolds containing either amniotic membrane powder or allantoin alone were also fabricated under the same optimized electrospinning parameters. For the third layer, a gelatin/carbomer blend was prepared by dissolving gelatin (30 wt%, corresponding to 1.8 g in 6 mL of 40% acetic acid) and carbomer (3.4 wt%, corresponding to 0.204 g in 6 mL) under continuous stirring to form a homogeneous viscous solution. The solution was electrospun to form the inner layer using the optimized parameters.

Characterization of fiber morphology and diameter by scanning electron microscopy (SEM)

The surface morphology of the electrospun scaffolds was evaluated by SEM at 25 kV. Before this examination, the samples were sputter-coated with a thin gold layer to enhance conductivity. SEM micrographs were acquired at appropriate magnifications to capture representative fiber morphology for each scaffold group. Representative SEM images of all scaffold groups are presented in Figure 1. Fiber diameters were quantified from SEM micrographs using ImageJ software (NIH, USA) by randomly selecting 50 fibers per scaffold group. Results are expressed as mean ± standard deviation (SD). Fiber diameter distributions for each group are presented as histograms in Supplementary Figure S1. Statistical differences in fiber diameter among the scaffold groups were assessed using one-way analysis of variance (ANOVA) followed by Tukey's honest significant difference (HSD) post hoc test for all pairwise comparisons. A value of $P \leq 0.05$ was considered statistically significant. A summary of mean fiber diameters and key statistical comparisons is provided in Table S1 (Supplementary file 1), and the complete set

Table 1. Composition of polymers, solvent systems, and electrospinning parameters used in the fabrication of the three-layer scaffold

Groups/conditions	Composition (wt%)	Solvent system	Electrospinning parameters
1	PU (12%)	THF/DMF (3:1)	14.5 kV, 0.2 mL h^{-1}, 300 rpm
2	PEO (12%) + Amniotic (1.5%) + Allantoin (0.75%)	Deionized water	14.5 kV, 0.2 mL h^{-1}, 300 rpm
3	Gelatin (30%) + Carbomer (3.4%)	Acetic acid (40%)	15.5 kV, 0.2 mL h^{-1}, 300 rpm

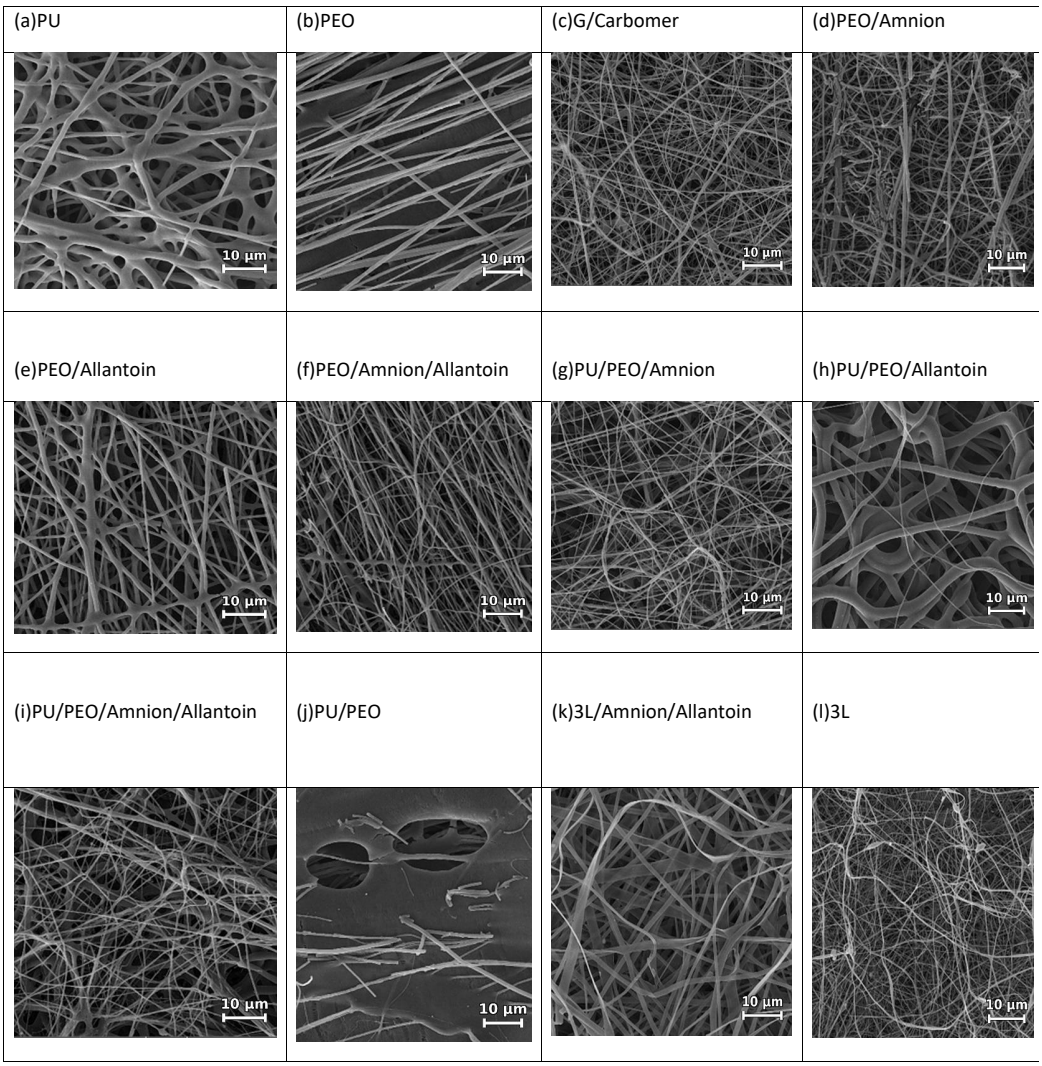


Figure 1. SEM micrographs of the electrospun nanofibrous layers (scale bar: 10 µm, magnification: 3.0 kx), (a) PU layer, (b) PEO layer, (c) G/Carbomer layer, (d) PEO/Amnion, (e) PEO/Allantoin, (f) PEO/Amnion/Allantoin, (g) PU/PEO/Amnion, (h) PU/PEO/Allantoin, (i) PU/PEO/Amnion/Allantoin,(j)PU/PEO,(k)PU/PEO/Amnion/Allantoin/GCarbomer(3L/Amnion/Allantoin) and (l) PU/PEO /G-Carbomer(3L).

of pairwise Tukey comparisons is presented in Table S2 (Supplementary file 1).

Tensile mechanical assay

The mechanical properties of the electrospun scaffolds were assessed by uniaxial tensile testing on a universal testing machine. Rectangular specimens (0.5×3 cm^2) were mounted in paper frames and extended at a constant crosshead speed of 5 mm/min until failure. Elastic modulus, ultimate tensile strength, and elongation at break were calculated from the stress–strain curves to evaluate scaffold strength and flexibility.

Water contact angle

Surface wettability of the scaffolds was determined by dynamic water contact angle measurements using a Krüss goniometer (Germany). Square samples (1×1 cm^2) of the scaffolds were fixed on a horizontal stage, and a 3 µL droplet of distilled water was deposited onto their surface. Contact angles were measured from droplet images after droplet stabilization using image analysis software. The evolution of the water contact angle was monitored from droplet deposition until droplet stabilization (approximately 60 s), and the values reported below represent the stabilized contact angle rather than the initial contact angle immediately after droplet placement.

Swelling ratio

The swelling capacity of the three-layer scaffolds was quantitatively evaluated by monitoring their weight variation in phosphate-buffered saline (PBS) (pH 7.4) at 37 °C under physiological conditions. The pre-weighed dry specimens (2×2 cm^2) from each scaffold group were immersed in PBS and incubated at 37 °C. At the predetermined time points, the samples were gently removed, dried with filter paper to remove excess surface liquid, and immediately weighed. The swelling ratio (%) was calculated using the following equation:

$$\text{Swelling ratio (\%)} = \frac{W_s - W_d}{W_d} \times 100$$

Where W_s and Wd represent the weights of the swollen and dry scaffolds, respectively.

Scaffold porosity

The surface porosity of the electrospun nanofibrous scaffolds and their individual layers was determined by image analysis of SEM micrographs using ImageJ software. At least five representative images per sample were processed. The images were converted to 8-bit grayscale and thresholded to produce binary images that clearly distinguished fibrous structures from pores. Scaffold porosity was calculated as the percentage of void area relative to the total area. The measurements were performed in triplicate (n = 3) and expressed as mean ± standard deviation.

Fourier-transform infrared spectroscopy (FTIR)

Functional chemical groups of the scaffolds were investigated by FTIR over the wavenumber range of 4000–400 cm^{-1}. Characteristic absorption peaks were detected to confirm the presence of polyurethane, polyethylene oxide, and carbomer/gelatin. Similarly, intermolecular interactions between the polymers and components were assessed from peak shifts and band broadening.

Release evaluation of amniotic membrane powder and allantoin

Specimens (1 × 1 cm^2) of each scaffold type were placed individually in 24-well plates containing 500 µL of PBS (pH 7.4) and incubated at 37 °C under continuous shaking at 100 rpm. At predetermined time intervals (6, 12, 24, 48, 72, 96, 120, 144, 168, 192, and 216 h), 100 µL aliquots of the release medium were withdrawn from each well and stored at −20 °C for subsequent analysis. Immediately after each withdrawal, 100 µL of fresh pre-warmed PBS was added to each well to maintain a constant volume. All experiments were performed in triplicate (n = 3). The concentration of released allantoin was determined by measuring the absorbance at 203 nm, and amniotic membrane powder-derived bioactive components were indirectly quantified by measuring the absorbance at 276 nm using the amniotic membrane powder extract (the same stock solution used for scaffold preparation) as the calibration standard, using a UV-Vis spectrophotometer. Standard calibration curves were prepared in PBS (pH 7.4) using pure allantoin for allantoin quantification, and the amniotic membrane powder extract itself for amniotic membrane powder-derived components. The theoretical loading of allantoin and amniotic membrane extract was defined according to the initial formulation composition. Encapsulation/loading efficiency was not directly determined in the present study. Since 20% of the release volume was removed at each sampling point, the cumulative amount of released compound was calculated using the following correction equation:

$$X'_n(t) = X_n(t) + 0.2 \times X'_{n-1}(t - \Delta t)$$

where $X'_n(t)$ is the corrected cumulative amount released at time t, $X_n(t)$ is the measured amount at time t, and X'_{n-1} is the corrected cumulative amount from the previous sampling point. Results are expressed as mean cumulative release (%) ± SD, and error bars in the release profiles represent the SD. The experimental release data were fitted to the following kinetic models using linear regression analysis:

Zero-order: $Q_t = Q_0 + k_0 t$
First-order: $\log(Q_\infty - Q_t) = \log Q_\infty - k_1 t$
Higuchi: $Q_t = k_H \sqrt{t}$
Korsmeyer–Peppas: $\frac{Q_t}{Q_\infty} = kt^n$

Goodness-of-fit was assessed using the coefficient of determination (R^2). The release exponent (n) from the Korsmeyer-Peppas model was used to characterize the release mechanism:

$n \leq 0.45$ indicates Fickian diffusion; $0.45 < n < 0.89$ indicates anomalous (non-Fickian) transport; $n = 0.89$ indicates Case II transport; and $n > 0.89$ indicates Super Case II transport.

Degradation assessment

In vitro degradation of the electrospun scaffolds was evaluated in PBS (pH 7.4) at 37 °C. Square specimens (1 × 1 cm^2) from each scaffold group were weighed (initial weight, M_0), immersed in PBS, and incubated for up to 60 days. At predetermined time points, samples were removed, rinsed with distilled water to eliminate residual salts, and dried to constant weight (remaining weight, M_t). The percentage weight loss (degradation rate) was calculated using the following equation:

$$\text{Degradation (\%)} = \frac{M_0 - M_t}{M_0} \times 100$$

Where M_0 and M_t represent the initial and remaining dry weights of the scaffolds, respectively.

MTT assay

Human fibroblast cells (Hu02) were cultured in DMEM/F12 medium supplemented with 10% FBS, 100 U/mL penicillin, and 100 µg/mL streptomycin under standard incubation conditions (37 °C, 5% CO_2). At approximately 90% confluence, the cells were detached with trypsin–EDTA and counted before seeding. For the MTT assay, scaffold samples were placed in 48-well tissue culture plates and seeded with cells under standard culture conditions. Three-layer scaffolds were sterilized by immersion in 70% ethanol, then exposed to ultraviolet (UV) light in a biosafety cabinet for 20 minutes, rinsed 3 times with PBS, and equilibrated in complete medium overnight. The cells were seeded onto the scaffolds at a density of 2.5×10^4 cells/cm^2, and the scaffolds were incubated in culture media every 2 days. Cell viability was evaluated at 1, 3, 7, and 14 days using the MTT assay (0.5 mg/mL; 4 h incubation). Formazan crystals were dissolved in 100 µL DMSO, and the absorbance values were quantified at 570 nm using a microplate reader.

DAPI staining

Cell attachment to the triple-layer scaffolds was evaluated by nuclear staining with 4′,6-diamidino-2-phenylindole (DAPI). For this method, the scaffold samples were cultured in 48-well tissue culture plates. After cell seeding at predetermined time points, the scaffolds were fixed, stained with DAPI, and imaged using a fluorescence microscope. Briefly, fibroblasts were seeded onto the scaffold at a density of 1×10^4 cells per well and were evaluated on days 1 and 14. At each time point, the samples were rinsed with PBS, fixed with 2% glutaraldehyde for 40 min, then serially dehydrated in ethanol (50%, 70%, 90%, and 100%), and incubated with DAPI in the dark for 5 min. After washing with PBS, the nuclei of the adhered cells were imaged using a fluorescence microscope.

Quantitative gene expression analysis

Quantitative real-time PCR (qRT-PCR) was performed to detect the expression of fibroblast migration- and angiogenesis-related genes, including discoidin domain receptor 2 (DDR2) and vascular endothelial growth factor (VEGF), in the cells cultured on different scaffold groups. After 3 days of incubation, total RNA was extracted using an isolation kit (Gibco, Iran) according to the manufacturer's protocol. Complementary DNA was then synthesized using a cDNA synthesis kit. qRT-PCR reactions were performed using a SYBR Green high-ROX master mix under the following thermal profile: initial denaturation at 95 °C for 10 min, followed by 40 amplification cycles at 95 °C for 15 s and 60 °C for 60 s. GAPDH was used as the internal reference gene, and relative mRNA expression values were quantified using the comparative ΔΔCt method. The primer sequences used for each target gene are listed in Table 2.

In vivo wound healing assessment

Adult male Wistar rats (8–10 weeks old; 250–300 g) were obtained from the Laboratory Animal Center of Tehran University (Tehran, Iran). All procedures were approved by the Institutional Ethics Committee of Shahid Beheshti University of Medical Sciences (Approval ID: IR.SBMU.AEC.1404.107) and carried out according to ARRIVE guidelines. After a 10-day acclimatization period under standard housing conditions, the rats were anesthetized with intraperitoneal ketamine (7 mg/kg) and xylazine (5 mg/kg). A single 1-cm full-thickness excisional wound was created on the dorsal midline using a sterile biopsy punch. Animals were randomized into 6 groups (n = 8 per group) as follows: (1) untreated wound (negative control); (2) three-layer scaffold seeded with fibroblasts; (3) scaffold containing fibroblasts and amniotic membrane powder; (4) scaffold containing fibroblasts and allantoin; (5) scaffold containing fibroblasts with the amniotic membrane powder/allantoin combination; (6) scaffold with amniotic membrane powder/allantoin without fibroblasts. The scaffolds were fixed using a semipermeable sterile bandage, and enrofloxacin (5 mg/kg/day) was administered subcutaneously to prevent infection. The macroscopic appearance and behavior of the wound were routinely observed. Wound size was evaluated on days 3, 7, 14, and 21 by digital imaging and quantified using ImageJ. The images were captured under consistent conditions (a fixed camera distance of 15 cm, a perpendicular angle to the wound surface, and uniform lighting) with a ruler placed close to each wound as a scale reference. Each group consisted of 12 animals (n = 12), with 3 animals evaluated at each time point.

Table 2. Primer sequences utilized for quantitative real-time PCR analysis

Gene	Primer sequence (5' → 3')
DDR2	**F:** GAGACCAAGGGAGGCAGAC
	R: CATCACTCGTCGCCTTGTTG
VEGF	**F:** CCCATGGCAGAAGGAGGAG
	R: GGATGGCTTGAAGATGTACTCG
GapdH	**F:** TCCTCCTGAGCGCAAGTAC
	R: CCTGCTTGCTGATCCACATCT

$$\text{Wound closure (\%)} = \left(1 - \frac{\text{Open wound area}}{\text{Initial wound area}}\right) \times 100$$

Histopathological analysis

At each time point, rats were euthanized with ketamine, and the wound tissues were collected and fixed in 10% neutral buffered formalin for 24 h. The specimens were embedded in paraffin, sectioned at 5 μm, and mounted on glass slides. Hematoxylin and Eosin (H&E) and Masson's trichrome (MT) staining were performed to evaluate inflammation, re-epithelialization, angiogenesis, and collagen deposition. The stained sections were examined under a digital light microscope. Inflammation, re-epithelialization, collagen deposition, and fibrosis were scored on a semiquantitative 0–4 scale. Three randomly selected sections from each animal were evaluated, and composite scores were summarized for 3 animals per group at each time point.

Statistical analysis

Unless otherwise specified, in vitro data were reported as mean ± SD from at least 3 independent replicates (n ≥ 3). Statistical analyses were performed using GraphPad Prism software (version 8.0). Differences between groups were evaluated using one-way or two-way ANOVA, followed by Tukey's post hoc multiple-comparison test. A value of $P \leq 0.05$ was considered statistically significant. For wound-closure and histopathological outcomes, 2 animals per group were analyzed separately at each time point using one-way ANOVA followed by Tukey's multiple-comparison test. Given the small number of animals at each time point, these inferential analyses were considered exploratory. Significance levels were denoted as follows: ns (not significant), *$P < 0.05$, ** $P < 0.01$, ****$P < 0.001$, and **** $P < 0.0001$.

Results

Fiber morphology and diameter of scaffolds

Scanning electron microscopy showed a porous,

interconnected nanofibrous architecture in all scaffold groups. Representative micrographs are shown in Figure S1. Fiber diameter differed significantly among the 7 scaffold groups (one-way ANOVA, $F(6, 338) = 307.71$, $P < 0.001$). The PU layer had the largest mean fiber diameter at 796.8 ± 123.6 nm (n = 50). The PEO layer had a mean diameter of 368.7 ± 58.8 nm (n = 50). The G/Carbomer layer had the smallest mean diameter among individual components at 268.6 ± 56.8 nm (n = 50). Incorporation of amniotic membrane powder into the PEO matrix did not significantly change fiber diameter (396.4 ± 74.3 nm vs. 368.7 ± 58.8 nm, Tukey HSD, $P = 0.52$). Addition of allantoin to the PEO matrix significantly reduced fiber diameter (307.2 ± 62.0 nm vs. 368.7 ± 58.8 nm, Tukey HSD, $P = 0.001$). The combined PEO/amnion/allantoin formulation had a mean diameter of 355.8 ± 59.6 nm, not significantly different from PEO alone (Tukey HSD, $P = 0.98$). Within the PEO-based intermediate layers, the PEO/amnion group differed significantly from the PEO/allantoin group (396.4 ± 74.3 nm vs. 307.2 ± 62.0 nm, Tukey HSD, $P < 0.001$). The PEO/allantoin group also differed significantly from the PEO/amnion/allantoin group (307.2 ± 62.0 nm vs. 355.8 ± 59.6 nm, Tukey HSD, $P = 0.02$). The PEO/amnion group did not differ significantly from the PEO/amnion/allantoin group (396.4 ± 74.3 nm vs. 355.8 ± 59.6 nm, Tukey HSD, $P = 0.09$). The control trilayer scaffold (PU/PEO/G-Carbomer) had a mean fiber diameter of 288.4 ± 50.5 nm (n = 50). This value was not significantly different from that of the G/Carbomer layer (268.6 ± 56.8 nm; Tukey HSD, $P = 0.83$). All pairwise comparisons against the PU layer were statistically significant (Tukey HSD, $P < 0.001$ for each), reflecting the markedly larger fiber diameter of PU relative to all other groups. Sequential SEM imaging showed continuous layer-by-layer deposition without visible interfacial delamination in the multilayer constructs. Measured fiber diameters for multilayer scaffolds corresponded to those of the exposed top layer. These observations indicated that incorporating amniotic membrane powder preserved the scaffold nanofiber morphology, whereas allantoin decreased fiber diameter.

Mechanical characteristics of scaffolds by tensile evaluation

Tensile testing was conducted to evaluate the mechanical performance of the electrospun scaffolds, with stress–strain curves shown in Figure 2A. All samples exhibited nonlinear viscoelastic behavior characterized by an initial elastic region, yielding, and subsequent failure. The control scaffold group (3L without bioactive additives) had an ultimate tensile strength of 28.80 MPa at 8.19% strain. When amniotic membrane powder was incorporated into the three-layer scaffold, the ultimate tensile strength was 23.82 MPa. The allantoin-containing scaffold exhibited an ultimate tensile strength of 36.53 MPa, while the combination of amniotic membrane powder and allantoin further increased the value to 38.19 MPa. The highest ultimate tensile strength of 38.19 MPa at 10.28% strain was obtained for the 3L/Amnion/Allantoin scaffold. Young's modulus, determined from the initial linear portion of the stress–strain curves, was 4.32 MPa for the control scaffold (3L), 11.06 MPa for the amnion-containing scaffold (3L/Amnion), 14.02 MPa for the amnion–allantoin scaffold (3L/Amnion/Allantoin), and 5.58 MPa for the allantoin-only scaffold (3L/Allantoin). The 3L/Allantoin scaffold exhibited higher ultimate tensile strength than the control (3L) and 3L/Amnion scaffolds, whereas the amnion-containing scaffolds showed higher Young's modulus than the control and allantoin-only scaffold.

Hydrophilicity of scaffolds by water contact angle measurements

The wettability of the three-layer scaffolds was evaluated by dynamic water contact angle measurements (Figure 2B). All formulations demonstrated hydrophilic character (contact angle < 90°), with marked differences among the variants (Figure 2C). The control scaffold (PU/PEO/Gelatin-Carbomer) exhibited a mean contact angle of 41° ± 2° (Figure 2B (a-b)). The incorporation of amniotic membrane powder into the intermediate PEO layer (PU/PEO(Amnion)/Gelatin-Carbomer) reduced the contact angle from 67° ± 1.5° to 34° ± 0.5° (Figure 2B (c-d)), indicating moderately enhanced surface hydrophilicity. The scaffold containing both amniotic membrane powder and allantoin (PU/PEO(Amnion–Allantoin)/Gelatin-Carbomer) displayed contact angles of 37° ± 1.1° (Figure 2B (e-f)), confirming preservation of hydrophilic behavior. Incorporating allantoin alone (PU/PEO(Allantoin)/Gelatin-Carbomer) resulted in greater droplet spreading and reached an angle of 0° (Figure 2B (g-h)), which indicated superhydrophilic behavior. These results indicated that allantoin promotes surface wettability, probably by introducing additional polar groups that facilitate rapid water penetration and spreading.

In vitro swelling behavior of scaffolds

The water absorption capacity of the scaffolds was studied in PBS at 37 °C (Figure 2D). All samples absorbed water rapidly during the first 20 min and then approached a near-equilibrium state, with no additional weight increase observed until 60 min. At equilibrium (20–60 min), the control scaffold showed a swelling ratio of approximately 218%. The incorporation of amniotic membrane powder alone increased the swelling ratio to 320%, consistent with the fluid-retaining capacity of the porous, hydrophilic amniotic membrane material. The scaffold containing only allantoin reached 378%, and the scaffold combining amniotic membrane and allantoin exhibited the highest value of 415%. The higher swelling in the modified scaffolds may have resulted from the strong water-attracting property of allantoin and the porous structure of the amniotic membrane powder. The increased water retention may help maintain a moist environment at the wound site, which is essential for healing, while rapid stabilization prevents over-swelling and tissue damage.

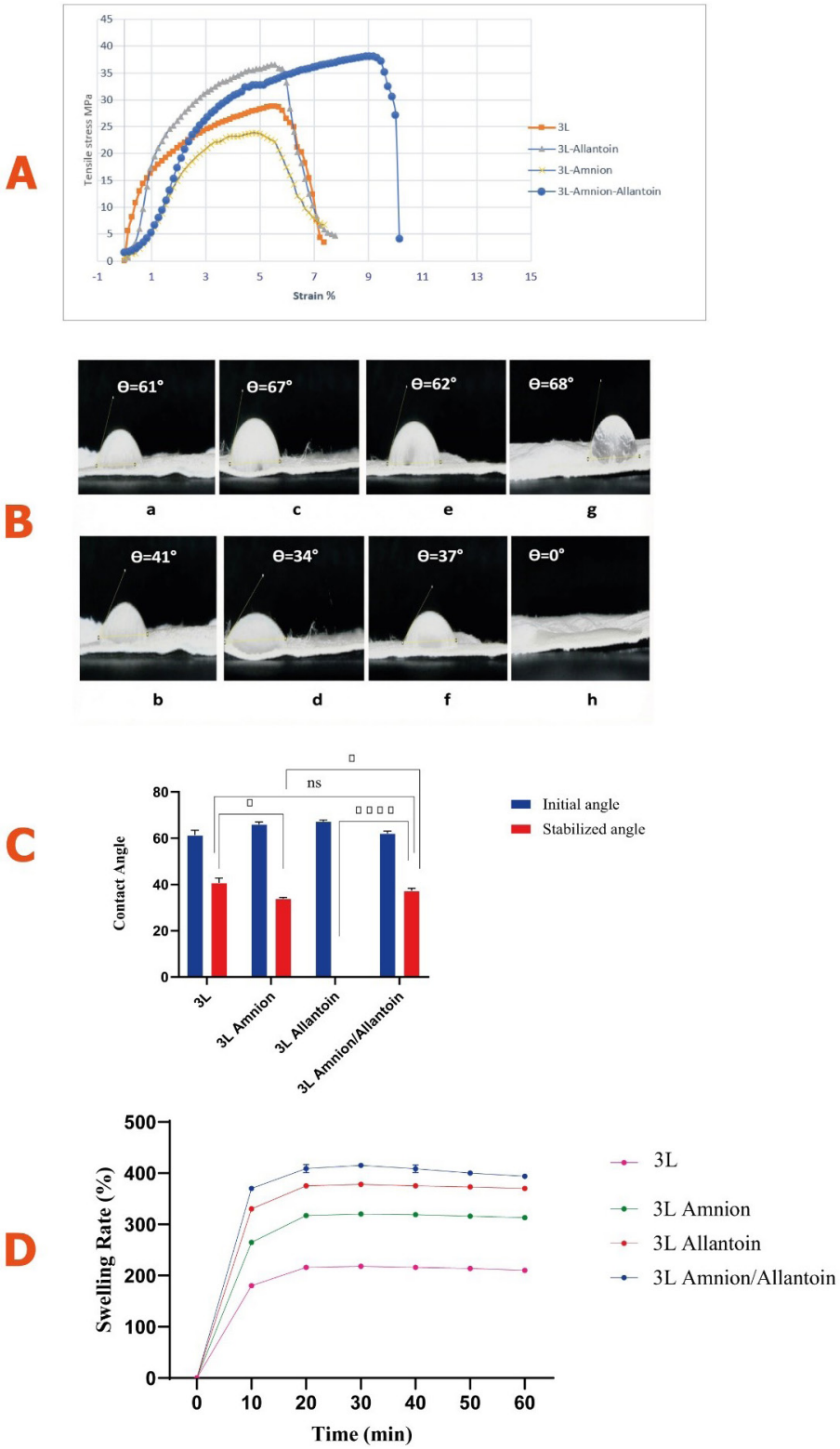


Figure 2. (A) Representative stress–strain curves of the three-layer (3L) electrospun scaffolds (3L, 3L/Allantoin, 3L/Amnion, and 3L/Amnion/Allantoin) obtained from uniaxial tensile testing. **(B)** Water contact angle measurements of the three-layer electrospun scaffolds using a 3 µL deionized water droplet (mean values derived from triplicate experiments; analysis performed using ImageJ). (a–b) 3L (PU/PEO/Gelatin–Carbomer): initial contact angle 61° and stabilized contact angle 41°. (c–d) 3L Amnion (PU/PEO(Amnion)/Gelatin–Carbomer): initial contact angle 67° and stabilized contact angle 34°. (e–f) 3L Amnion/Allantoin (PU/PEO(Amnion–Allantoin)/Gelatin–Carbomer): initial contact angle 62° and stabilized contact angle 37°. (g–h) 3L Allantoin (PU/PEO(Allantoin)/Gelatin–Carbomer): initial contact angle 68° and stabilized contact angle 0°. **(C)** Results of Tukey's multiple comparisons test for water contact angles at the initial and stabilized measurement points. Data are reported as mean ± SD (n = 3). *P < 0.05, ****P < 0.0001; ns, not significant. **(D)** Swelling ratios (%) of the three-layer electrospun nanofiber scaffolds (control and modified variants) in phosphate-buffered saline (PBS, pH 7.4) over 60 min.

Determination of porosity value of scaffolds

Porosity analysis of the electrospun nanofibrous scaffolds and their individual layers was conducted using ImageJ software. The PU base layer exhibited a porosity of 45 ± 5%, reflecting its dense, compact fibrous structure (Figure 3A). The relatively low porosity of the PU layer

was consistent with its role as structural support within the multilayer scaffold. In comparison, the PEO intermediate layer exhibited higher porosity of 60 ± 5% ($P < 0.05$ vs. PU). The finer fibers and lower packing density in this layer created larger void spaces that may facilitate nutrient diffusion and cellular infiltration, key factors in

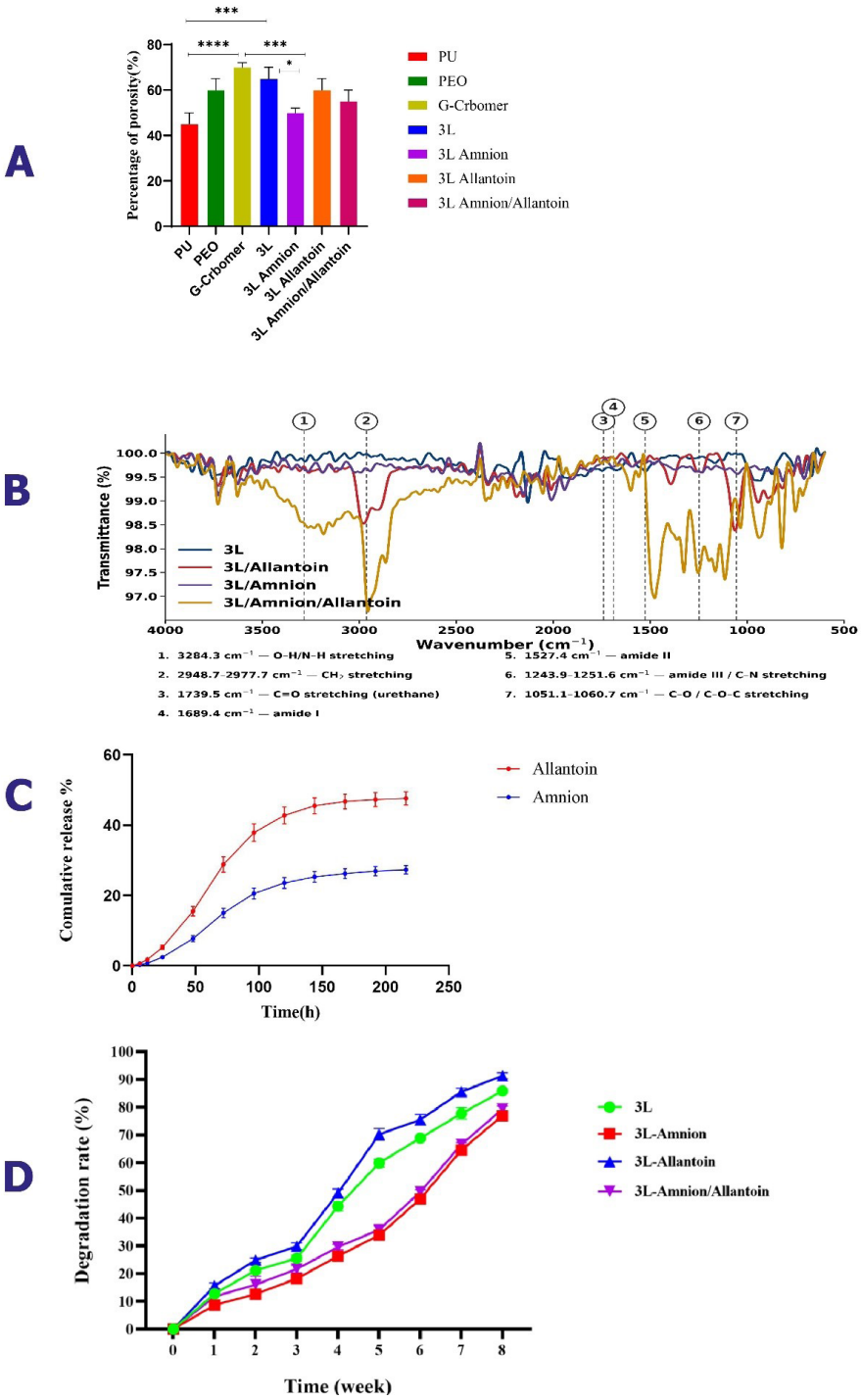


Figure 3. (A) Porosity percentages of the electrospun nanofibrous layers and three-layer scaffolds, as determined by ImageJ analysis (mean ± SD; n = 3). The data highlight a porosity gradient from the dense PU base layer to the highly porous G/Carbomer top layer, with bioactive additives in the intermediate layer modulating overall scaffold porosity. (*$P < 0.05$, ***$P < 0.001$, ****$P < 0.0001$; ns: not significant), (B) FTIR spectra of the pristine three-layer scaffold (3L) and three-layer scaffolds containing allantoin, amniotic membrane powder, or both components. Amniotic membrane powder denotes amniotic membrane powder incorporated into the scaffold. The numbered reference lines denote the characteristic bands identified from the experimental spectra: (1) 3284.3 cm^{-1}, O–H/N–H stretching; (2) 2948.7–2977.7 cm^{-1}, CH_2 stretching; (3) 1739.5 cm^{-1}, C = O stretching; (4) 1689.4 cm^{-1}, amide I; (5) 1527.4 cm^{-1}, amide II; (6) 1243.9–1251.6 cm^{-1}, amide III/C–N stretching; and (7) 1051.1–1060.7 cm^{-1}, C–O/C–O–C stretching. The reference lines denote assigned band positions; individual bands may not be detectable in every spectrum, (C) Cumulative in vitro release of allantoin (203 nm) and amniotic membrane components (276 nm) from three-layer electrospun scaffolds containing these bioactive agents in the intermediate PEO layer (3L/Allantoin and 3L/Amnion, respectively) and (D) In vitro degradation profiles of the three-layer (3L) electrospun scaffolds (3L, 3L/Amnion, 3L/Allantoin, and 3L/Amnion/Allantoin) over 60 days in PBS (pH 7.4) at 37 °C. The data are reported as percentage weight loss (mean ± SD, n = 3). The 3L and 3L/Allantoin scaffolds had faster degradation, whereas the amnion-containing scaffolds showed significantly slower degradation.

tissue regeneration. The gelatin/carbomer (G/Carbomer) inner wound-contact layer displayed the highest porosity among the single layers, reaching 70 ± 5% ($P < 0.0001$ vs. PU). Its loose and irregular fiber arrangement produced an open, highly permeable network that supports moisture retention and effective interaction with the wound bed. Among the three-layer scaffolds, the control variant (PU/PEO/G-Carbomer) had a surface porosity of 65 ± 5%. The scaffold incorporating amniotic membrane powder in the intermediate layer (PU/PEO-Amnion/G-Carbomer) showed reduced porosity of 50 ± 5%, which was significantly lower than both the control ($P < 0.05$) and the standalone G/Carbomer layer ($P < 0.001$). This decrease may be attributed to local densification caused by the amniotic particles. In contrast, the scaffold containing allantoin in the intermediate layer (PU/PEO-Allantoin/G-Carbomer) had a porosity of 60 ± 5%, which did not differ significantly from that of the control or the non-loaded PEO layer. The complete scaffold containing both amniotic membrane powder and allantoin in the intermediate layer (PU/PEO-Amnion-Allantoin/G-Carbomer) presented an intermediate porosity of 55 ± 5%, which was significantly lower than the G/Carbomer layer ($P < 0.05$), in contrast to the control scaffold. Collectively, the porosity values ranged from 45% to 70% between the different layers and scaffold groups. This pore-size gradient resembled the natural architecture of skin tissue, influencing cell migration, proliferation, and new tissue formation while maintaining sufficient mechanical stability and appropriate hydration conditions.

Detection of functional chemical groups of scaffolds by FTIR analysis

FTIR spectroscopy identified the characteristic functional groups of the fabricated scaffolds (Figure 3B and Figures S4–S6). The PU layer showed absorption bands at 1728.0 cm^{-1} (C = O stretching of urethane groups), 1112.8 cm^{-1} (C–O–C stretching), and 2950.7 cm^{-1} (CH_2 stretching).[40]

The pure PEO layer displayed bands at 2916.0 cm^{-1} (CH_2 stretching) and 1060.7 cm^{-1} (C–O–C ether stretching), consistent with previous reports.[41, 42]

The pure Carbomer/Gelatin layer exhibited bands at 1242.0 cm^{-1} (amide III), 2979.6 cm^{-1} (CH_2 stretching), and 1060.7 cm^{-1} (C–O stretching).[43, 44]

The U/PEO scaffold retained the characteristic PU carbonyl band at 1733.8 cm^{-1} and exhibited additional absorption bands at 2923.7 cm^{-1}, assigned to CH_2 stretching, and 1060.7 cm^{-1}, assigned to C–O–C ether stretching.

The U/PEO/Allantoin scaffold exhibited bands at 1728.0 cm^{-1} (C = O stretching), 1560.2 cm^{-1} (N–H bending), 1249.7 cm^{-1} (C–N stretching), and 2948.7 cm^{-1} (CH_2 stretching), consistent with the ureide structure of allantoin.[45]

The U/PEO/Amnion scaffold showed bands at 1722.2 cm^{-1} (C = O stretching), 1243.9 cm^{-1} (amide III), 3409.7 cm^{-1} (N–H stretching), and 2968.0 cm^{-1} (CH_2 stretching).[43]

The U/PEO/Amnion/Allantoin scaffold exhibited bands at 1722.2 cm^{-1} (C = O stretching), 1506.2 cm^{-1} (N–H bending), and 2983.5 cm^{-1} and 2879.3 cm^{-1} (CH_2 stretching).

The pristine three-layer scaffold (3L) showed a broad band at 3284.3 cm^{-1} (O–H/N–H stretching) and a band at 1527.4 cm^{-1} (amide II). The 3L/Allantoin scaffold exhibited bands at 1243.9 cm^{-1} (C–N stretching), 2977.7 cm^{-1} (CH_2 stretching), and 1060.7 cm^{-1} (C–O–C stretching), confirming allantoin incorporation. The 3L/Amnion scaffold showed bands at 1689.4 cm^{-1} (amide I), 1243.9 cm^{-1} (amide III), and 1051.1 cm^{-1} (C–O stretching). The 3L/Amnion/Allantoin scaffold exhibited bands at 1739.5 cm^{-1} (C = O stretching), 1251.6 cm^{-1} (amide III), and 2948.7 cm^{-1} (CH_2 stretching).

The PEO/Allantoin control exhibited bands at 1533.2 cm^{-1} (N–H bending) and 3481.0 cm^{-1} and 3392.3 cm^{-1} (N–H stretching), confirming the characteristic functional groups of allantoin. The PEO/Amnion control showed bands at 1687.5 cm^{-1} (amide I) and 2944.9 cm^{-1} (CH_2 stretching). The PEO/Amnion/Allantoin control exhibited bands at 1261.3 cm^{-1} (amide III), 2925.6 cm^{-1} (CH_2 stretching), and 1062.6 cm^{-1} (C–O–C stretching).[43,44]

The characteristic absorption bands of polyurethane, PEO, carbomer/gelatin, amniotic membrane, and allantoin were retained across all composite scaffolds. Slight shifts in peak position and band broadening were observed among formulations, consistent with intermolecular hydrogen-bonding interactions between scaffold components. No additional absorption bands were detected, suggesting that FTIR did not identify new covalent bonds and that interactions among the constituents were predominantly physical.[40,45,46]

Cumulative release profiles of amniotic membrane powder-derived bioactive components and allantoin from the scaffolds

The in vitro cumulative release profiles of allantoin and soluble amniotic membrane powder-derived bioactive components from the polymeric scaffolds over 216 h are shown in Figure 3C. Both systems displayed a sustained-release pattern with no pronounced initial burst. Allantoin reached a cumulative release of 28.80 ± 2.20% at 72 h, progressively increasing to 47.60 ± 1.90% at 216 h. Amniotic membrane powder-derived bioactive components showed a comparatively attenuated profile, reaching 15.00 ± 1.40% at 72 h and 27.30 ± 1.20% at 216 h (mean ± SD, n = 3). The lower overall release extent of amniotic membrane powder-derived components is consistent with the greater molecular complexity and size heterogeneity of the amniotic membrane powder matrix constituents, which encounter greater steric and diffusional resistance within the polymeric network. Release kinetics were analyzed by fitting the cumulative release data to zero-order, first-order, Higuchi, and Korsmeyer-Peppas models. The kinetic parameters, equations, correlation coefficients (R^2), and mechanistic interpretations are

summarised in Table 3 (allantoin) and Table 4 (amniotic membrane powder-derived components). Kinetic model fitting plots (zero-order, first-order, Higuchi, and Korsmeyer–Peppas) for both compounds are provided in Figures S2–S3 (Supplementary file 1).

Allantoin release kinetics

Kinetic model fitting results for allantoin release are presented in Table 3.

The Higuchi model showed the best fit with the highest R^2 (0.9403), indicating that allantoin release is primarily controlled by diffusion through the polymeric matrix. The Korsmeyer–Peppas model also provided a good fit ($R^2 = 0.9197$) with a release exponent $n = 0.8493$, which falls within the range $0.45 < n < 0.89$, indicating anomalous (non-Fickian) transport, in which both molecular diffusion and polymer chain relaxation/swelling contribute to the release process. The zero-order model provided a relatively good fit ($R^2 = 0.8933$), suggesting a partial contribution from matrix swelling and/or erosion, whereas the first-order model showed a weak correlation ($R^2 = 0.6726$), suggesting concentration-dependent release as the primary mechanism. Generally, allantoin release followed a diffusion-dominated, non-Fickian mechanism with a secondary contribution from polymer relaxation within the scaffolds.

Amniotic membrane powder-derived bioactive component release kinetics

Kinetic model fitting results for Amniotic membrane powder-derived bioactive components are presented in Table 4.

The Korsmeyer–Peppas model provided the best fit ($R^2 = 0.9665$) with a release exponent $n = 1.3235$, which exceeds 1.0 and thus classifies the transport mechanism as Super Case II. This mechanism is dominated by polymer chain relaxation, matrix swelling, structural reorganization, and erosion rather than Fickian diffusion. The Higuchi model also detected a strong correlation ($R^2 = 0.9419$), confirming a significant diffusive contribution to the release process. However, the superior fit of the Korsmeyer-Peppas model indicated that diffusion alone did not fully explain the observed release behavior. The zero-order model provided a good fit ($R^2 = 0.9120$), consistent with a partially controlled-release profile. The first-order model showed the lowest R^2 (0.7287), indicating that the release rate is not governed by the residual concentration of the bioactive components within the matrix. The allantoin release obeyed a diffusion-dominated, non-Fickian mechanism, whereas amniotic membrane powder-derived component release was primarily governed by Super Case II transport (matrix relaxation and erosion), with a secondary contribution from diffusion. These results indicated sustained release of both bioactive agents, which is desirable for tissue engineering and wound-healing applications.

In vitro degradation of scaffolds

Degradation behavior of the electrospun scaffolds was evaluated in PBS (pH 7.4) at 37 °C for 60 days (Figure 3D). The bioactive-free 3L scaffold degraded most rapidly, reaching approximately 50% weight loss by week 4. The 3L/Allantoin scaffold exhibited slightly faster degradation, achieving 50% weight loss in the 3–4 week range, due to the increased hydrophilicity provided by allantoin. In contrast, scaffolds incorporating amniotic membrane powder degraded considerably more slowly. The 3L/Amnion scaffold reached 50% weight loss after 7 weeks, while the 3L/Amnion/Allantoin scaffold showed a comparable degradation behavior, reaching 50% mass loss slightly earlier, around weeks 6–7. These results indicated slower degradation in the amnion-containing scaffolds and faster degradation in the allantoin-containing scaffold.

Cell viability of scaffolds

Fibroblast viability on the three-layer nanofibrous scaffolds was assessed using an MTT assay over 14 days (Figure 4A). The tested scaffolds included a bioactive-free control (PU/PEO/G-Carbomer), scaffolds containing amniotic membrane powder (PU/PEO/Amnion/G-Carbomer), allantoin (PU/PEO/Allantoin/G-Carbomer), or their combination (PU/PEO/Amnion/Allantoin/G-Carbomer). They were compared with tissue culture

Table 3. Kinetic model parameters for the in vitro release of allantoin from the scaffold (n = 3)

Kinetic Model	Equation	R^2	Interpretation
Zero-order	y = 0.259x + 3.7031	0.8933	Relatively good fit; matrix swelling and/or erosion contribute to release
First-order	y = 0.0056x + 0.7568	0.6726	Poor fit; concentration-dependent release is not the dominant mechanism
Higuchi	y = 4.1939x − 7.7195	0.9403	Best fit; diffusion-controlled release through the polymeric matrix
Korsmeyer–Peppas	y = 0.8493x − 0.2281	0.9197	n = 0.8493 → Anomalous (non-Fickian) transport; diffusion and polymer relaxation both contribute

Table 4. Kinetic model parameters for the in vitro release of Amniotic membrane powder-derived bioactive components from the scaffold (n = 3)

Kinetic Model	Equation	R^2	Interpretation
Zero-order	y = 0.1492x + 1.4963	0.9120	Good fit; sustained release with possible contribution of matrix erosion and swelling
First-order	y = 0.0081x + 0.1252	0.7287	Poor fit; concentration-dependent release is not the dominant mechanism
Higuchi	y = 2.3934x − 4.8934	0.9419	Good fit; diffusion contributes significantly to the release process
Korsmeyer–Peppas	y = 1.3235x − 1.4454	0.9665	Best fit; n = 1.3235 → Super Case II transport; polymer relaxation, swelling, and matrix erosion dominate

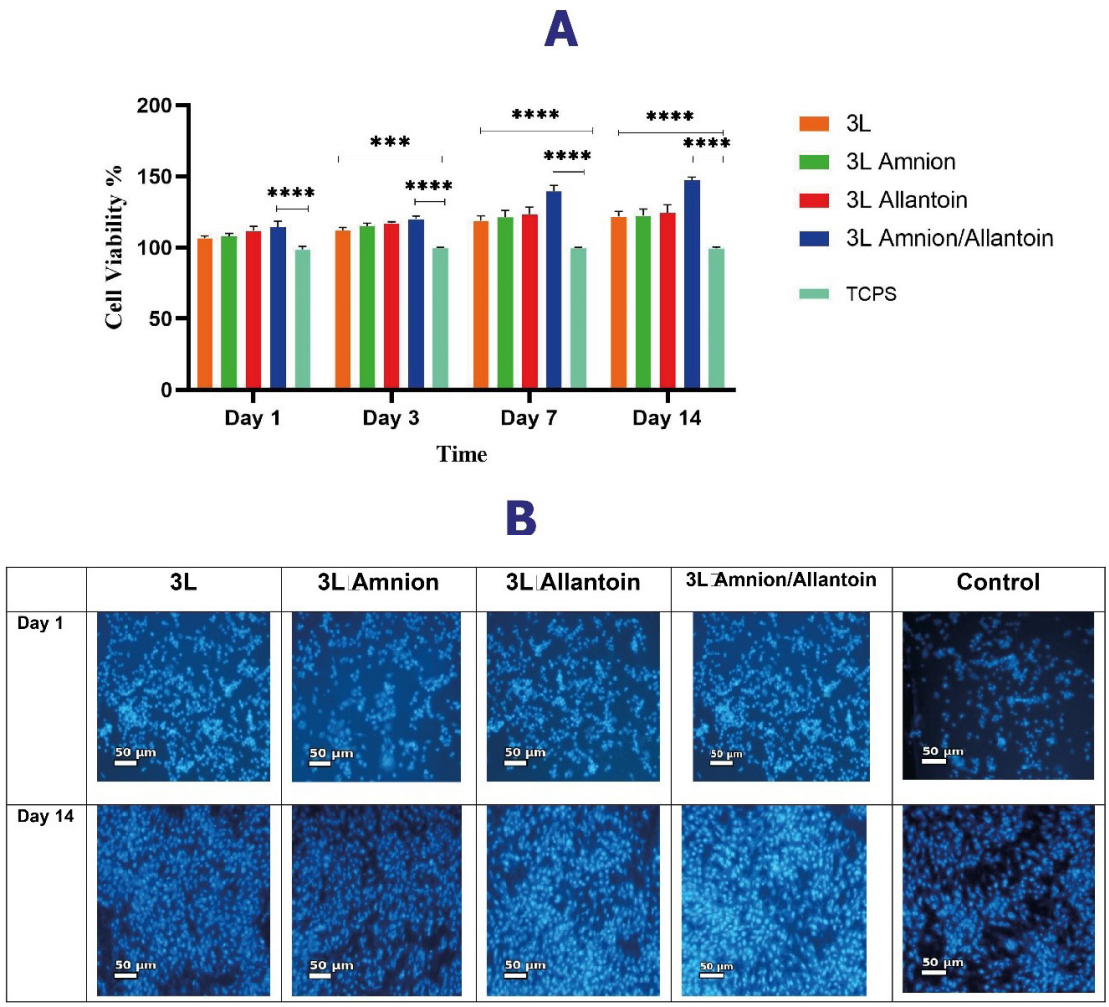


Figure 4. (A) Fibroblast cell viability (%) on the three-layer (3L) electrospun scaffolds (3L, 3L/Amnion, 3L/Allantoin, and 3L/Amnion/Allantoin) and the tissue culture polystyrene (TCPS) control over 14 days, as determined by the MTT assay. Data are presented as mean ± SD (n = 3). ***P* < 0.01, ****P* < 0.001, *****P* < 0.0001. **(B)** Fluorescence microscopy images of DAPI-stained fibroblasts cultured on the three-layer (3L) electrospun scaffolds at 1 and 14 days after cell seeding. Columns represent the experimental groups: 3L (PU/PEO/Gelatin-Carbomer), 3L/Amnion, 3L/Allantoin, 3L/Amnion/Allantoin, and the tissue culture polystyrene (TCPS) control. Blue fluorescence indicates cell nuclei. Bioactive-loaded scaffolds exhibited enhanced cell attachment and a more homogeneous cell distribution over time compared with the TCPS control. Scale bar = 50 µm.

polystyrene (TCPS), which served as the control. After 1 day, all scaffold groups demonstrated higher cell viability than TCPS, indicating favorable early cell attachment. The scaffold containing both amniotic membrane powder and allantoin exhibited significantly greater viability compared with PU/PEO/G-Carbomer ($P = 0.0402$) and TCPS ($P < 0.0001$). Scaffolds incorporating a single bioactive component also showed improved viability relative to TCPS ($P < 0.01$ to $P < 0.0001$), with no significant differences among them. By day 3, cell viability continued to increase across all experimental groups. The PU/PEO/Amnion/Allantoin/G-Carbomer scaffold maintained significantly higher viability than PU/PEO/G-Carbomer ($P = 0.0293$) and TCPS ($P < 0.0001$). All bioactive-containing scaffolds showed higher viability than TCPS ($P < 0.0001$), while remaining statistically comparable to each other. At day 7, a clear distinction between scaffold compositions became evident. The combined amnion/allantoin scaffold showed significantly higher fibroblast viability than PU/PEO/G-Carbomer, PU/PEO/Amnion/G-Carbomer, PU/PEO/Allantoin/G-Carbomer, and TCPS (all $P < 0.0001$). Scaffolds containing either amniotic membrane powder or allantoin alone supported similar levels of viability and remained superior to the controls. After 14 days, the PU/PEO/Amnion/Allantoin/G-Carbomer scaffold continued to exhibit significantly higher cell viability than all other groups ($P < 0.0001$). Scaffolds containing a single bioactive component sustained higher viability than TCPS ($P < 0.0001$) but did not differ significantly from each other. According to the cytotoxicity grading system reported by Liu et al., these values correspond to first-grade cytotoxicity.[47] Fibroblast viability was highest on the scaffold containing both amniotic membrane powder and allantoin at days 7 and 14. The viability results are presented in Figure 4A.

Fluorescence imaging of fibroblast attachment and distribution

Fluorescence imaging was used to assess fibroblast attachment and distribution across various scaffold

formulations, with DAPI staining to highlight cell nuclei (Figure 4B). After 1 day, the cells expanded across all groups. The control group showed minimal attachment and faint blue fluorescence, consistent with limited cell adhesion. In contrast, the bioactive-free three-layer (3L) scaffold exhibited moderate cell clustering, while the scaffolds containing amniotic membrane powder and allantoin showed denser nuclear staining, consistent with greater initial cell attachment. By day 14, greater cell density and a more uniform distribution were observed in the treated groups, particularly in the 3L/Amnion/Allantoin scaffold, where intense blue fluorescence covered the scaffold surface, consistent with greater cell coverage. The scaffold containing both allantoin and amniotic membrane powder showed greater cell coverage than the control on day 14.

SEM of fibroblast morphology

SEM was used to examine fibroblast attachment and morphology on the nanofibrous scaffolds after 14 days of cell seeding (Figure 5A). These results demonstrated firm cell adhesion to the scaffold surface in all scaffold groups. Fibroblasts exhibited extensive spreading on the nanofibers, indicating effective cell-scaffold interactions. The cells displayed spindle-like morphologies, a characteristic of healthy fibroblasts. The corresponding cell shape displayed filopodia and lamellipodia, which helped them attach to the fibrous matrix. Moreover, close cell–cell contacts were observed, suggesting cellular organization on the scaffold surface.

SEM showed attached fibroblasts on the interconnected porous architecture, without visible regions of cell detachment or surface incompatibility. Together, the SEM findings showed that the electrospun three-layer scaffold provided support for fibroblast adhesion and morphological integrity. These observations were consistent with the fibroblast-viability findings.

Gene expression analysis

Quantitative real-time PCR (qRT-PCR) was performed to evaluate the mRNA expression levels of vascular endothelial growth factor (VEGF), a key angiogenic marker, and discoidin domain receptor 2 (DDR2), which is involved in cell migration and extracellular matrix remodeling, in Hu02 fibroblasts three days after cell seeding (Figure 5B). The highest expression levels of both VEGF and DDR2 were observed in the 3L/Amnion/Allantoin scaffold. VEGF expression in this group was approximately two-fold higher than that in the bioactive-free 3L scaffold ($P<0.01$) and significantly higher than that in the tissue culture polystyrene (TCPS) control ($P<0.001$). The scaffolds containing either amniotic membrane or allantoin alone exhibited modest enhancements in VEGF expression (approximately 1.2-fold and 1.3-fold, respectively), although these differences were statistically insignificant compared with the bioactive-free 3L scaffold. For DDR2, the 3L/Amnion/Allantoin scaffold exhibited the highest expression level

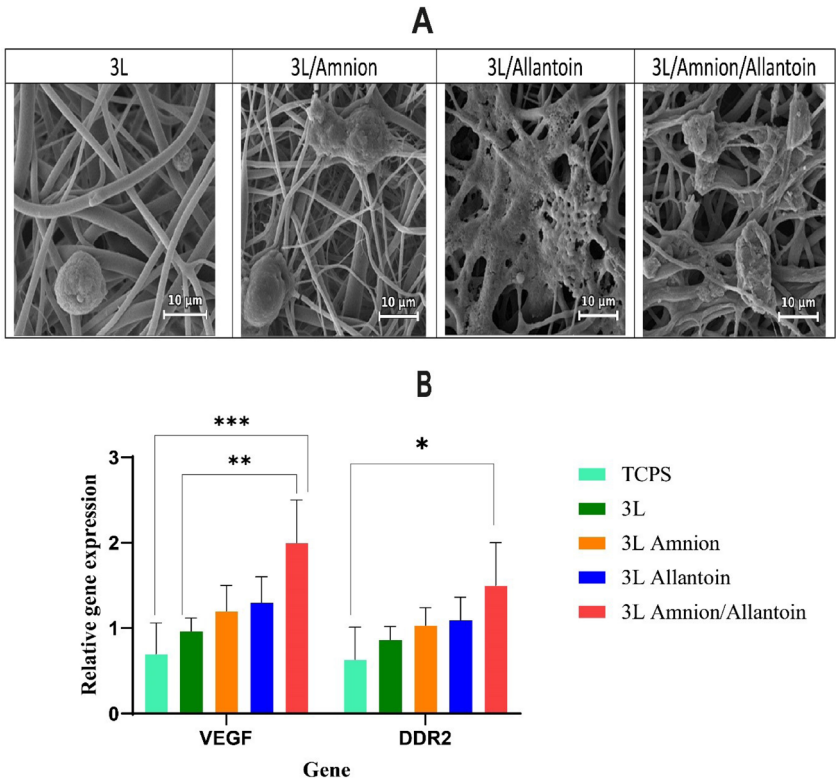


Figure 5. (A) SEM images of Hu02 fibroblasts cultured on the three-layer (3L) electrospun nanofibrous scaffolds (3L, 3L/Amnion, 3L/Allantoin, and 3L/Amnion/Allantoin) after 14 days of culture. Cells exhibited firm attachment and an elongated morphology on the fibrous surface. All images were acquired at a magnification corresponding to a 10 µm scale bar. **(B)** Quantitative real-time PCR (qRT-PCR) analysis of VEGF and DDR2 gene expression in fibroblasts cultured on the three-layer (3L) electrospun scaffolds. The 3L/Amnion/Allantoin scaffold exhibited enhanced expression of both genes compared with the tissue culture polystyrene (TCPS) control.

among all experimental groups and showed a significant increase compared with the TCPS control ($P<0.05$), whereas no statistically significant difference was observed relative to the bioactive-free 3L scaffold. These results showed that the combined formulation altered the expression of genes associated with angiogenesis and extracellular-matrix remodeling.

In vivo wound healing assessment

The efficacy of fibroblast, amniotic membrane powder, and allantoin combinations on the PU/PEO/G-Carbomer wound scaffold was assessed in the control and treated groups using a full-thickness wound model in rats. All scaffold groups were applied to the wound sites, and the healing process was observed over 21 days. Quantitative wound closure data for all groups at each time point are presented in Table S4. There were no significant differences in body weight between the groups. During the study, all rats remained healthy; 3 rats per group were euthanized at each time point for histological assessment. The wound closure percentage was calculated relative to the initial area on day 1 and to measurements of their size at specific time points (days 3, 7, 14, and 21 post-injury). Figure 6A presents wound photographs for each treatment group at the post-wounding stages indicated.

Figure 6B shows the wound closure percentages. On day 3, similar open wounds were seen in all groups, and wound closure remained limited. After 7 days, the treated groups collectively demonstrated significant reductions in wound size compared with the control, particularly in the 3L/Fibroblast/Amnion/Allantoin group, which showed the greatest contraction (50.0 ± 1.0%, $P<0.0001$ vs. control). The 3L/Fibroblast/Amnion/Allantoin group also showed greater closure than 3L/Fibroblast (30.0 ± 2.0%, $P<0.0001$) or 3L/Fibroblast/Allantoin (35.0 ± 2.0%, $P<0.0001$). The 3L/Fibroblast/Amnion/Allantoin group had the highest mean wound closure on day 7. On day 14, the treated groups showed higher closure than the control, with the highest closure in the 3L/Fibroblast/Amnion/Allantoin group (90.0 ± 1.0%, $P<0.0001$ vs. the control). Closure in this group was greater than in the 3L/Fibroblast/Amnion group (80.0 ± 1.0%, $P<0.0001$) and the 3L/Amnion/Allantoin group (85.0 ± 1.0%, $P<0.0006$). No significant difference was found between the 3L/Fibroblast/Amnion and 3L/Fibroblast/Allantoin groups. By day 21, wound closure reached at least 99% in all groups, with no significant intergroup differences.

Histological evaluation of in vivo wound healing assessment

Histological analysis of wound tissues stained with H&E and MT was performed on days 3, 7, 14, and 21 post-wounding to evaluate the progression of tissue repair among the six experimental groups (Figures 7 (H&E) and 8 (MT)). Histological scoring was performed using a semi-quantitative scale (0–4) for inflammation, re-epithelialization, collagen deposition, and fibrosis (Table S5). Three randomly selected histological sections were evaluated per animal (n = 3 animals per group at each time point). On day 3, hematoxylin and eosin staining across all groups showed similar acute wound responses, characterized by disrupted epidermal layers, extensive infiltration of inflammatory cells, including neutrophils and macrophages, and fibrin clots with minimal granulation tissue formation. The inflammation score on day 3 was uniformly high across all groups, with no significant intergroup differences ($P>0.05$). In contrast, Masson's trichrome staining detected immature collagen fibers in blue, dominated by red-stained muscle and cytoplasmic components, indicating the early inflammatory phase without significant matrix remodeling in the control, 3L/Fibroblast, 3L/Fibroblast/Allantoin, 3L/Fibroblast/Amnion, 3L/Fibroblast/Amnion/Allantoin, and 3L/Amnion/Allantoin groups. The collagen deposition score on day 3 was minimal in all groups. After 7 days, the control group showed persistent inflammation with scattered inflammatory cells and initial granulation tissue in H&E sections accompanied by limited blue collagen fibers in MT staining (inflammation score: 3.0 ± 0.4; re-epithelialization: 1.0 ± 0.2; collagen: 1.5 ± 0.3), whereas the 3L/Fibroblast group had reduced inflammation (2.0 ± 0.3, $P<0.05$ vs. control), early re-epithelialization at wound edges, a modest increase in collagen deposition and a mild increase in newly formed vessels compared with the control; the 3L/Fibroblast/Allantoin group showed even lower inflammation, partial epithelial bridging, and greater organized early collagen fibers and a further increase in vascular density; the 3L/Fibroblast/Amnion group depicted considerable decreases in infiltrates, advancing re-epithelialization, and denser collagen bundles; the 3L/Fibroblast/Amnion/Allantoin group showed the most advanced repair with minimal inflammation, extensive epithelial migration, and stronger blue-stained collagen indicating active remodeling and the highest degree of vascularization among all groups, with well-organized blood vessels throughout the granulation tissue, whereas the 3L/Amnion/Allantoin group showed lowered inflammation (1.0 ± 0.3, $P<0.01$ vs. control), good epithelial coverage, and enhanced collagen formation compared to the control. On day 14, H&E staining in the control revealed moderate inflammation, incomplete re-epithelialization, and low granulation tissue and a disorganized vascular network. MT staining in this group also showed weak collagen deposition.

In contrast, the 3L/Fibroblast group had reduced inflammation, near-complete epithelial layers, and better-aligned collagen fibers (3.0 ± 0.3), as well as an increased number of mature vessels at the wound margins. The 3L/Fibroblast/Allantoin group possessed minimal residual inflammation, fully formed epithelium, and compact collagen deposition. On the other hand, the 3L/Fibroblast/Amnion group showed better tissue organization, thin epithelial coverage, and dense collagen deposition, which was stained blue. The 3L/Fibroblast/Amnion/Allantoin group exhibited highly mature structures with no visible

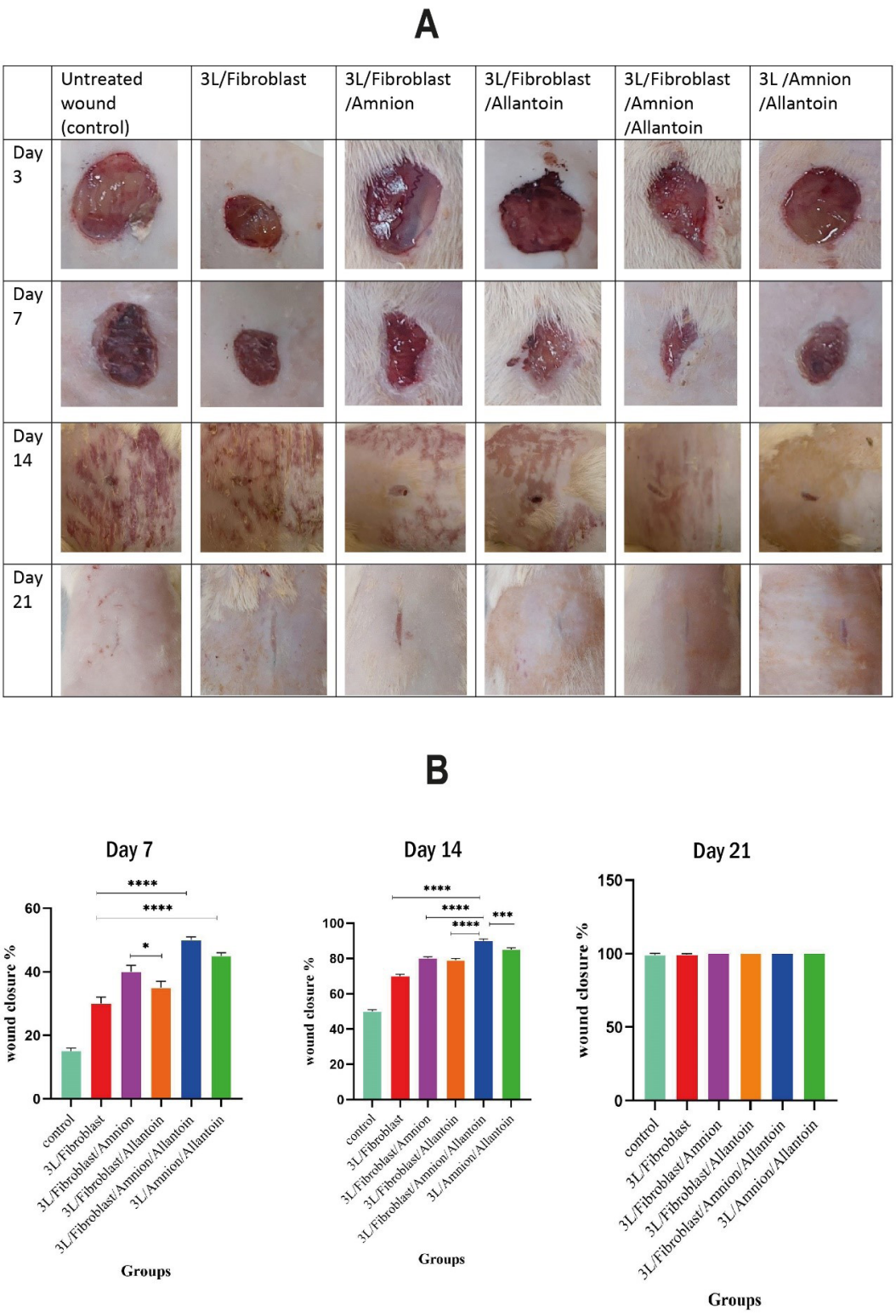


Figure 6. (A) Representative macroscopic images of wounds in rats during the 21-day healing period. The rows represent wound appearance on days 3, 7, 14, and 21 and the columns correspond to the following experimental groups: Untreated wound (control), 3L/Fibroblast (PU/PEO-Fibroblast/G-Carbomer),3L/Fibroblast/Amnion(PU/PEO-Fibroblast-Amnion/G-Carbomer),3L/Fibroblast/Allantoin(PU/PEO-Fibroblast-Allantoin/G-Carbomer), 3L/Fibroblast/Amnion/Allantoin(PU/PEO-Fibroblast-Amnion-Allantoin/G-Carbomer), and 3L/Amnion/Allantoin (PU/PEO-Amnion-Allantoin/G-Carbomer). **(B)** Quantitative analysis of wound closure after 3, 7, 14, and 21 days, calibrated with the percentage of the original wound area. The data are presented as mean ± SD (n = 3 animals per group at each time point). ns, not significant; *$P < 0.05$; ***$P < 0.001$; ****$P < 0.0001$.

inflammation, showed advanced re-epithelialization and well-structured collagen bundles. The 3L/Amnion/Allantoin group displayed similar maturity, with organized tissue and reduced collagen remodeling. After 21 days, all groups showed complete re-epithelialization on H&E sections, but the control group had thicker scars and an irregular dermal structure, with extensive fibrosis on MT staining. The 3L/Fibroblast group presented thinner scars and a more uniform dermis with balanced collagen. The 3L/Fibroblast/Allantoin group showed

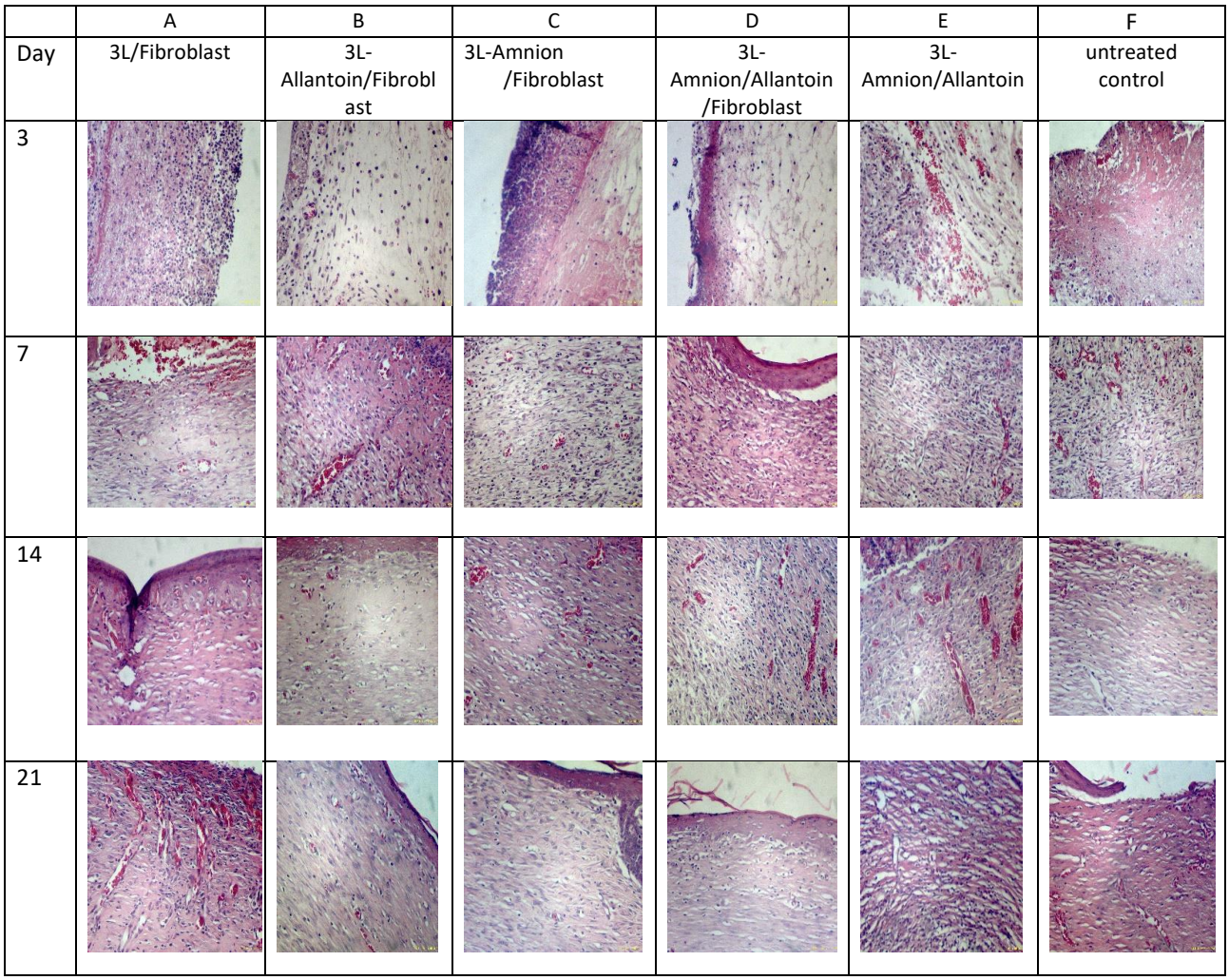


Figure 7. Representative hematoxylin and eosin (H&E)-stained sections of full-thickness skin wounds from the experimental groups (a–f) on days 3, 7, 14, and 21 post-injury. The groups were as follows: (a) 3L/Fibroblast, (b) 3L/Fibroblast/Allantoin, (c) 3L/Fibroblast/Amnion, (d) 3L/Fibroblast/Amnion/Allantoin, (e) 3L/Amnion/Allantoin, and (f) untreated control. The images illustrate the temporal progression of wound healing, including inflammatory cell infiltration, re-epithelialization, granulation tissue formation, fibroblast proliferation, and angiogenesis.

well-organized tissue with minimal scarring and even collagen distribution. Similarly, the 3L/Fibroblast/Amnion group showed smooth integration and low fibrosis (fibrosis: 1.0 ± 0.2, $P < 0.01$ vs. control), while the 3L/Fibroblast/Amnion/Allantoin group showed the most favorable histological appearance, with a natural-like skin structure and the least fibrosis (fibrosis: 0.5 ± 0.2, $P < 0.001$ vs. control). Histological appearance differed among the experimental groups. The 3L/Amnion/Allantoin group also exhibited advanced remodeling with small scars and mature, aligned collagen fibers. The wound-healing histopathological scores of the experimental groups on days 3, 7, 14, and 21 are presented in Figure S7.

Discussion

Chronic wound healing is characterized by prolonged inflammation, insufficient angiogenesis, and impaired extracellular matrix remodeling, creating a poor cellular environment. Therefore, creating a scaffold with a better cellular environment and providing mechanical support are necessary for advanced wound scaffolds that can actively support tissue regeneration.[48] Electrospun nanofibrous scaffolds offer an approach to address these challenges by more closely mimicking the fibrillar architecture of the native skin ECM. Moreover, this similarity typically provides high porosity and an interconnected pore architecture, facilitating cell adhesion and proliferation while supporting cell migration and efficient nutrient exchange within the wound region.[49] This fabrication approach also enables the incorporation of bioactive agents in a relatively simple and controllable manner, allowing their gradual release at the wound site. At the same time, the resulting nanofibrous structure can help maintain moisture at the wound surface by absorbing wound exudate, thereby supporting the different stages of the healing process.[50, 51]. In accordance with these criteria, the present study developed a three-layer electrospun scaffold to promote ECM organization and provide sufficient mechanical properties. Morphological evaluation confirmed a porous, bead-free fibrous structure in all layers, a feature expected to promote cell attachment and growth while enabling efficient nutrient transport throughout the scaffold.[52] The absence of visible interlayer separation indicated continuous interfaces after sequential

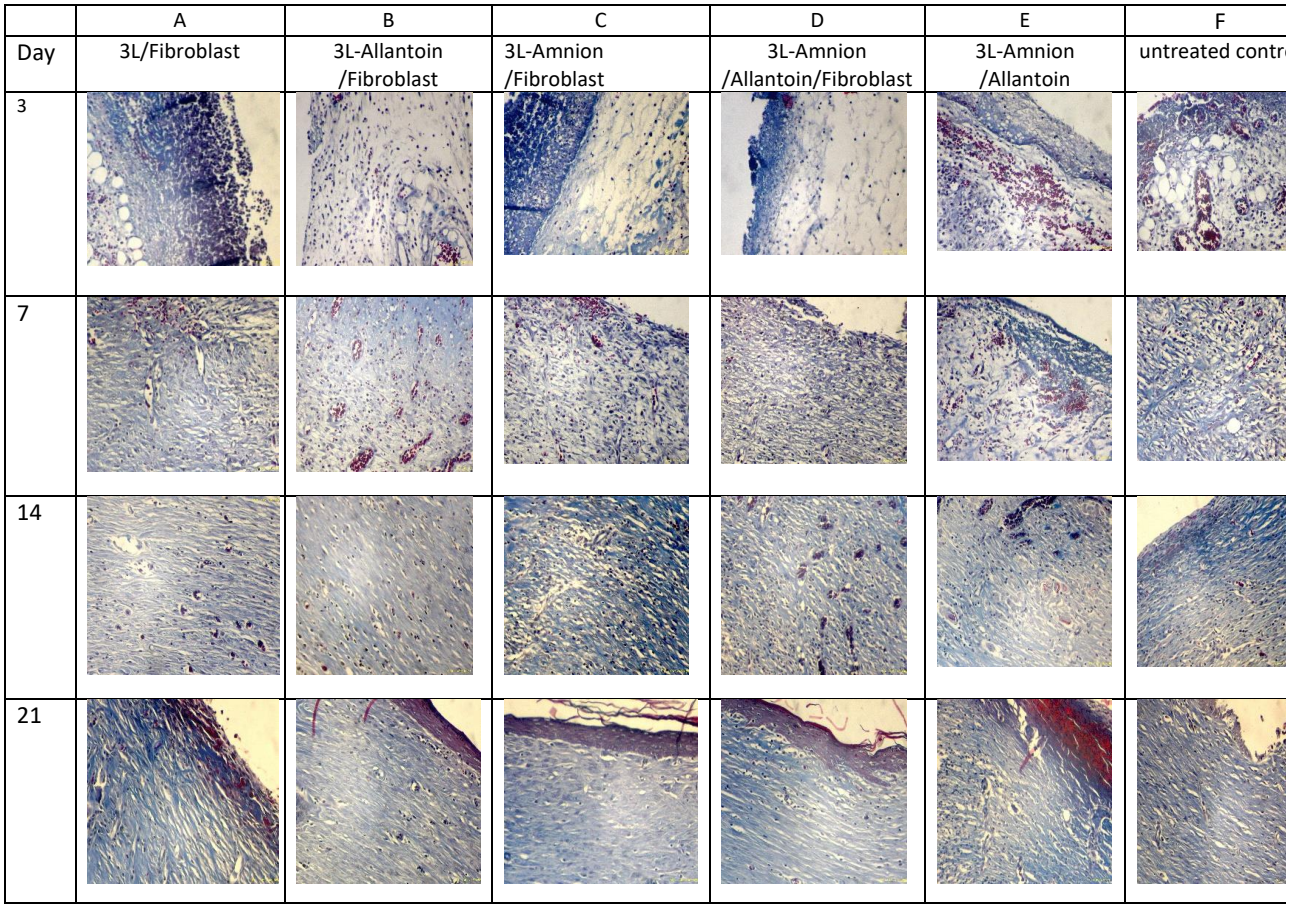


Figure 8. Representative Masson's trichrome-stained sections of full-thickness skin wounds from the experimental groups (a–f) on days 3, 7, 14, and 21 post-injury. The groups were as follows: (a) 3L/Fibroblast, (b) 3L/Fibroblast/Allantoin, (c) 3L/Fibroblast/Amnion, (d) 3L/Fibroblast/Amnion/Allantoin, (e) 3L/Amnion/Allantoin, and (f) untreated control. The images illustrate collagen deposition, fiber organization, and extracellular matrix maturation during the wound-healing process.

electrospinning; interfacial strength was not measured directly. In the intermediate PEO layer, incorporation of amniotic membrane powder produced a nonsignificant numerical increase in fiber diameter relative to pure PEO. This pattern may be related to increased solution viscosity, which can restrict jet stretching during electrospinning and promote thicker fibers.[53] Fiber uniformity was maintained. In contrast, the presence of amniotic membrane–derived particles on the fiber surface may mediate anti-inflammatory and regenerative responses, in agreement with the well-documented biological activity of amniotic membrane components.[54] In contrast, incorporation of allantoin alone led to a reduction in fiber diameter, which is likely related to the increase in solution conductivity. Higher conductivity enhances jet elongation during electrospinning, thereby favoring the formation of thinner fibers.[53] When both amniotic membrane powder and allantoin were incorporated, an intermediate fiber diameter was obtained, which likely reflects the competing effects of increased solution viscosity and conductivity on jet dynamics, as has been reported for similar blend electrospinning solutions.[55] The mechanical properties of native human skin vary with anatomical site and testing conditions. In general, the ultimate tensile strength of native human skin is reported to range from approximately 5 to 30 MPa, while Young's modulus varies from about 0.1–1 MPa at low strain levels to roughly 5–30 MPa under uniaxial tensile loading conditions.[56] All scaffold groups in the present study exhibited nonlinear viscoelastic behavior within or near reported mechanical ranges for native human skin. A previous study reported a tensile strength of approximately 8.5 MPa for an amniotic membrane-based scaffold, indicating that incorporation of amniotic membrane can influence scaffold mechanical behavior.[57] Previous studies have shown that electrospun polymeric scaffolds containing allantoin can modify tensile behavior by enhancing flexibility while maintaining adequate mechanical integrity, which is consistent with the lower Young's modulus and relatively high tensile strength observed for the allantoin-containing scaffold in the present study.[29] The novelty of the present scaffold architecture was further highlighted by comparison with previously reported electrospun wound dressings (Table S3). Previous studies have investigated multilayer electrospun systems based on combinations such as polyurethane and gelatin, or incorporated individual bioactive components including amniotic membrane derivatives or allantoin into electrospun matrices.[30, 58, 59] Unlike these reported systems, the current three-layer scaffold integrated polyurethane, polyethylene oxide, carbomer/gelatin, amniotic membrane powder, and allantoin within distinct layers to provide combined

mechanical support and bioactive delivery functions. FTIR analysis confirmed successful incorporation of amniotic membrane powder and allantoin via their characteristic bands.[40-45] Slight shifts in O–H/N–H stretching and carbonyl regions, plus band broadening, suggested intermolecular hydrogen-bonding interactions among polyurethane, PEO, carbomer, gelatin, amniotic membrane components, and allantoin. These interactions are typical in physically blended polymeric systems and may improve component compatibility without altering chemical structures. No new absorption bands were detected, suggesting that FTIR did not identify new covalent bonds or chemical crosslinking.[46, 60] Such physical interactions may contribute to the observed improvements in scaffold hydrophilicity and fibroblast behavior [54, 61]

The enhanced fibroblast viability, attachment, and functional activity observed on the three-layer scaffold (3L/Fibroblast/Amnion/Allantoin group) suggest combined effects of the scaffold components. This result is further supported by evidence showing cell-based scaffolds can enhance therapeutic outcomes by providing a supportive microenvironment for cellular functions.[60] Recent research has reported that amniotic membrane–based scaffolds promote cell adhesion and survival through the presence of growth factors, extracellular matrix proteins, and anti-inflammatory mediators.[54, 62] At the same time, allantoin has been shown to enhance fibroblast proliferation and tissue regeneration by stimulating cellular metabolism and migration.[27, 29] Furthermore, bioactive electrospun membranes have also been reported to support cell seeding and viability.[63] SEM observations showed spindle-shaped fibroblast morphology and stable cell–scaffold contact on the electrospun nanofibrous scaffold.[64] Moreover, gene-expression analysis showed that the 3L/Amnion/Allantoin scaffold increased VEGF expression relative to the bioactive-free 3L scaffold and TCPS. DDR2 expression was higher than in TCPS but did not differ significantly from the bioactive-free 3L scaffold. DDR2 is activated by direct interaction with ECM collagen and triggers extracellular signal-regulated kinase 1/2 (ERK1/2) signaling pathways to promote fibroblast migration and collagen remodeling during wound repair.[65] In addition, DDR2–collagen interactions regulate fibroblast migration and extracellular matrix remodeling, partly through transcriptional activation of matrix metalloproteinases, further supporting the role of DDR2 in ECM organization.[66] In parallel, fibroblast-derived VEGF has been shown to directly stimulate endothelial cell recruitment and neovascularization, thereby accelerating angiogenesis during wound repair.[67] Hypoxia and extracellular matrix–mediated interactions further activate hypoxia-inducible factor 1-alpha (HIF-1α) signaling in fibroblasts, leading to increased VEGF expression and more angiogenic activity.[68] The measured expression profile was consistent with pathways involved in fibroblast migration, matrix remodeling, and angiogenesis, although these functional effects were not measured directly. The treated groups showed faster wound contraction and improved histological maturation compared with the control. The 3L/Fibroblast/Amnion/Allantoin group showed the most rapid closure and the most organized tissue formation; these changes were accompanied by reduced inflammation and more advanced tissue repair. Resolution of inflammation is associated with the transition to fibroblast proliferation and extracellular-matrix deposition during wound repair.69 Amniotic membrane powder-containing scaffolds reduce inflammatory infiltration and enhance re-epithelialization. This result is in agreement with another study that reported that dehydrated human amnion/chorion grafts modulate inflammatory responses and promote epithelial migration during wound healing.[70] The significant epithelial coverage observed by days 7–14 is consistent with the proliferative phase during wound healing models such as in rodents. Accordingly, granulation tissue formation and re-epithelialization occurred within the first 2 weeks after injury.[71] During the remodeling phase, the 3L/Fibroblast/Amnion/Allantoin group showed more organized collagen deposition and lower fibrosis than the control, as assessed by Masson's trichrome staining. These findings are consistent with previous *in vivo* observations showing that allantoin-based wound scaffolds enhance collagen maturation and accelerate tissue regeneration in rat models. [72] In general, the combined 3L/Fibroblast/Amnion/Allantoin scaffold improved healing kinetics and scar architecture. [73] Several limitations of the present study should be acknowledged. The in vivo experimental timeline was confined to a 21-day observation period, which, although adequate for characterizing the early and proliferative phases of cutaneous wound healing, including granulation tissue formation, re-epithelialization, and preliminary collagen deposition, does not encompass the full continuum of the tissue repair process. The present investigation did not incorporate long-term histological follow-up to assess chronic inflammatory reactions or later scar-tissue remodeling. These outcomes are relevant to the long-term quality of wound repair and functional tissue restoration. Longer follow-up would therefore be required to assess extracellular matrix remodeling, collagen-fiber reorganization, biocompatibility, structural integration, and functional durability in vivo. Taken together, the integration of fibroblasts, amniotic membrane powder, and allantoin within a nanofibrous scaffold provided a supportive microenvironment for wound repair. The findings support further evaluation of the scaffold and its components for dermal regeneration.

Conclusion

In this study, a three-layer electrospun nanofibrous scaffold composed of PU, PEO, and carbomer/gelatin layers, loaded with amniotic membrane powder and allantoin, was developed as a wound scaffold. The 3L/Amnion/Allantoin scaffold showed favorable mechanical properties, hydration, and sustained release, and it

supported fibroblast attachment and viability. *VEGF expression was higher than in the bioactive-free 3L scaffold and TCPS, whereas DDR2 expression was higher than in TCPS but not significantly different from the bioactive-free scaffold. In vivo assessments showed earlier wound closure through day 14. The 3L/Fibroblast/Amnion/Allantoin group also showed greater epithelial coverage, more organized collagen deposition, and less fibrosis than the untreated control.* These outcomes supported the combined use of amniotic membrane powder and allantoin within the nanofibrous architecture. The scaffold combined mechanical support with local delivery of the bioactive components and supported fibroblast viability. The findings support further evaluation of the 3L/Fibroblast/Amnion/Allantoin scaffold for skin repair. Future studies of this scaffold should focus on longer-term evaluations and mechanistic pathways to assess its suitability for clinical translation.

Authors' Contribution

Conceptualization: Simzar Hosseinzadeh.
Data curation: Nahid Heidari Hafshejani, Simzar Hosseinzadeh.
Formal analysis: Nahid Heidari Hafshejani, Simzar Hosseinzadeh.
Funding acquisition: Simzar Hosseinzadeh, Bahram Kazemi.
Investigation: Nahid Heidari Hafshejani, Azam Rahimpour, Hojjat Allah Abbaszadeh, Hojatollah Montazeri, Sepideh Ghani.
Methodology: Nahid Heidari Hafshejani, Simzar Hosseinzadeh.
Project administration: Simzar Hosseinzadeh.
Resources: Simzar Hosseinzadeh, Nahid Heidari Hafshejani.
Supervision: Simzar Hosseinzadeh.
Validation: Simzar Hosseinzadeh.
Visualization: Nahid Heidari Hafshejani.
Writing-original draft: Nahid Heidari Hafshejani.
Writing–review & editing: Simzar Hosseinzadeh, Bahram Kazemi.

Competing Interests

None declared.

Ethical Approval

This study was approved by Shahid Beheshti University of Medical Sciences, with the ethical codes of IR.SBMU.REC.1404.107 and IR.SBMU.AEC.1405.016.

Funding

This study was conducted under a grant from the School of Advanced Technologies in Medicine, Shahid Beheshti University of Medical Sciences (grant number: 43018558)

Supplementary Files

Supplementary file 1 contains Tables S1-S5 and Figures S1-S7.

References

1. Gray M, Black JM, Baharestani MM, Bliss DZ, Colwell JC, Goldberg M, et al. Moisture-associated skin damage: overview and pathophysiology. J Wound Ostomy Continence Nurs 2011; 38: 233-41. doi:10.1097/WON.0b013e318215f798
2. Diller RB, Tabor AJ. The role of the extracellular matrix (ECM) in wound healing: a review. Biomimetics (Basel) 2022; 7: 87. doi:10.3390/biomimetics7030087
3. Dong R, Guo B. Smart wound dressings for wound healing. Nano Today 2021; 41: 101290. doi:10.1016/j.nantod.2021.101290
4. Li X, Xue X, Xie P. Smart dressings and their applications in chronic wound management. Cell Biochem Biophys 2024; 82: 1965-77. doi:10.1007/s12013-024-01402-w
5. Gupta MN, Rangaraju A, Ambre P. Sustainable dressings for wound healing. Biotechnol Sustain Mater 2025; 2: 1. doi:10.1186/s44316-024-00023-w
6. Li S, Li L, Guo C, Qin H, Yu X. A promising wound dressing material with excellent cytocompatibility and proangiogenesis action for wound healing: strontium loaded silk fibroin/sodium alginate (SF/SA) blend films. Int J Biol Macromol 2017; 104: 969-78. doi:10.1016/j.ijbiomac.2017.07.020
7. Andreu V, Mendoza G, Arruebo M, Irusta S. Smart dressings based on nanostructured fibers containing natural origin antimicrobial, anti-inflammatory, and regenerative compounds. Materials (Basel) 2015; 8: 5154-93. doi:10.3390/ma8085154
8. Jiang Z, Zheng Z, Yu S, Gao Y, Ma J, Huang L, et al. Nanofiber scaffolds as drug delivery systems promoting wound healing. Pharmaceutics 2023; 15: 1829. doi:10.3390/pharmaceutics15071829
9. Venugopal J, Low S, Choon AT, Ramakrishna S. Interaction of cells and nanofiber scaffolds in tissue engineering. J Biomed Mater Res B Appl Biomater 2008; 84: 34-48. doi:10.1002/jbm.b.30841
10. Liu M, Duan XP, Li YM, Yang DP, Long YZ. Electrospun nanofibers for wound healing. Mater Sci Eng C Mater Biol Appl 2017; 76: 1413-23. doi:10.1016/j.msec.2017.03.034
11. Wang Y, Yue G, Lu H, Liu Z, Wang N, Liu F, et al. Wound dressing applications of electrospun nanofibers: mechanism, construction and recent progress. Nanoscale 2026; 18: 6203-20. doi:10.1039/d5nr04448k
12. Kubera Sampath Kumar S, Prakash C, Vaidheeswaran S, Karthic Kumar B, Subramanian S. Design and characterization of secondary and tertiary layers of a multilayer wound dressing system. J Test Eval 2020; 48: 2683-98. doi:10.1520/jte20180199
13. Song J, Gao Z, Zhang Y, Li Y, Zhao Y, Yan H, et al. Bioinspired electrospun Janus nanofibrous dressing for synergistic antibacterial activity and tissue regeneration. Front Microbiol 2026; 17: 1788110. doi:10.3389/fmicb.2026.1788110
14. Doostmohammadi M, Niknezhad SV, Foroootanfar H, Ghasemi Y, Jafari E, Adeli-Sardou M, et al. Development of Ag NPs/allantoin loaded PCL/GEL electrospun nanofibers for topical wound treatment. J Biomater Appl 2023; 38: 692-706. doi:10.1177/08853282231212605
15. Zainab I, Naseem Z, Batool SR, Waqas M, Nazir A, Nazeer MA. Polyurethane/silk fibroin-based electrospun membranes for wound healing and skin substitute applications. Beilstein J Nanotechnol 2025; 16: 591-612. doi:10.3762/bjnano.16.46
16. Ferreira CA, Januário AP, Félix R, Alves N, Lemos MF, Dias JR. Multifunctional gelatin/chitosan electrospun wound dressing dopped with *Undaria pinnatifida* phlorotannin-enriched extract for skin regeneration. Pharmaceutics 2021; 13: 2152. doi:10.3390/pharmaceutics13122152
17. Menon A, Sreeram P, Vinod A, Naiker V, Nandana MV, David DA, et al. Polyurethane (PU): structure, properties, and applications. In: Raghavan P, Sreekala MS, Ravindran L, Menon A, eds. Handbook of Thermosetting Foams, Aerogels, and Hydrogels. Elsevier; 2024. p. 67-92. doi:10.1016/b978-0-323-99452-1.00001-2
18. Chen KS, Leon Yu T, Chen YS, Lin TL, Liu WJ. Soft-and hard-segment phase segregation of polyester-based polyurethane. J Polym Res 2001; 8: 99-109. doi:10.1007/s10965-006-0139-3
19. Xu R, Xia H, He W, Li Z, Zhao J, Liu B, et al. Controlled water vapor transmission rate promotes wound-healing via wound re-epithelialization and contraction enhancement. Sci Rep 2016; 6: 24596. doi:10.1038/srep24596
20. Gharibi R, Yeganeh H, Rezapour-Lactoee A, Hassan ZM. Stimulation of wound healing by electroactive, antibacterial, and antioxidant polyurethane/siloxane dressing membranes: in vitro and in vivo evaluations. ACS Appl Mater Interfaces 2015; 7: 24296-311. doi:10.1021/acsami.5b08376
21. Uscátegui YL, Díaz LE, Valero MF. In vitro and in vivo biocompatibility of polyurethanes synthesized with castor oil polyols for biomedical devices. J Mater Res 2019; 34: 519-31. doi:10.1557/jmr.2018.448
22. Morales-Gonzalez M, Arévalo-Alquichire S, Diaz LE, Sans JÁ, Vilariño-Feltrer G, Gómez-Tejedor JA, et al. Hydrolytic stability and biocompatibility on smooth muscle cells of polyethylene glycol–polycaprolactone-based polyurethanes. J Mater Res 2020; 35: 3276-85. doi:10.1557/jmr.2020.303
23. Gaydhane MK, Sharma CS, Majumdar S. Electrospun nanofibres in drug delivery: advances in controlled release strategies. RSC

Adv 2023; 13: 7312-28. doi:10.1039/d2ra06023j
24. Ramakrishna S, Fujihara K, Teo WE, Yong T, Ma Z, Ramaseshan R. Electrospun nanofibers: solving global issues. Mater Today 2006; 9: 40-50. doi:10.1016/s1369-7021(06)71389-x
25. Raihan MT, Mahmud MH, Mazumder BC, Chowdhury MN, Islam MT. A review of PEO (polyethylene oxide) assisted electrospinning of chitosan: innovation, production, and application. J Polym Mater 2025; 42: 677-711. doi:10.32604/jpm.2025.068356
26. Pakravan M, Heuzey MC, Ajji A. Core-shell structured PEO-chitosan nanofibers by coaxial electrospinning. Biomacromolecules 2012; 13: 412-21. doi:10.1021/bm201444v
27. Araújo LU, Grabe-Guimarães A, Mosqueira VC, Carneiro CM, Silva-Barcellos NM. Profile of wound healing process induced by allantoin. Acta Cir Bras 2010; 25: 460-6. doi:10.1590/s0102-86502010000500014
28. Xie H, Bai Q, Kong F, Li Y, Zha X, Zhang L, et al. Allantoin-functionalized silk fibroin/sodium alginate transparent scaffold for cutaneous wound healing. Int J Biol Macromol 2022; 207: 859-72. doi:10.1016/j.ijbiomac.2022.03.147
29. Dorri Nokoorani Y, Shamloo A, Bahadoran M, Moravvej H. Fabrication and characterization of scaffolds containing different amounts of allantoin for skin tissue engineering. Sci Rep 2021; 11: 16164. doi:10.1038/s41598-021-95763-4
30. Lotfi Z, Khakbiz M, Davari N, Bonakdar S, Mohammadi J, Shokrgozar MA, et al. Fabrication and multiscale modeling of polycaprolactone/amniotic membrane electrospun nanofiber scaffolds for wound healing. Artif Organs 2023; 47: 1267-84. doi:10.1111/aor.14518
31. Munoz-Torres JR, Martínez-González SB, Lozano-Luján AD, Martínez-Vázquez MC, Velasco-Elizondo P, Garza-Veloz I, et al. Biological properties and surgical applications of the human amniotic membrane. Front Bioeng Biotechnol 2022; 10: 1067480. doi:10.3389/fbioe.2022.1067480
32. Maljaars LP, Bendaoud S, Kastelein AW, Guler Z, Hooijmans CR, Roovers JW. Application of amniotic membranes in reconstructive surgery of internal organs-a systematic review and meta-analysis. J Tissue Eng Regen Med 2022; 16: 1069-90. doi:10.1002/term.3357
33. Vaseashta A, Salel S, Bölgen N. Biopolymer-based electrospun nanofibers for wound healing, regeneration, and therapeutics. Materials (Basel) 2026; 19: 1443. doi:10.3390/ma19071443
34. Malafaya PB, Silva GA, Reis RL. Natural-origin polymers as carriers and scaffolds for biomolecules and cell delivery in tissue engineering applications. Adv Drug Deliv Rev 2007; 59: 207-33. doi:10.1016/j.addr.2007.03.012
35. Ndlovu SP, Ngece K, Alven S, Aderibigbe BA. Gelatin-based hybrid scaffolds: promising wound dressings. Polymers (Basel) 2021; 13: 2959. doi:10.3390/polym13172959
36. Gomes SR, Rodrigues G, Martins GG, Roberto MA, Mafra M, Henriques CM, et al. In vitro and in vivo evaluation of electrospun nanofibers of PCL, chitosan and gelatin: a comparative study. Mater Sci Eng C Mater Biol Appl 2015; 46: 348-58. doi:10.1016/j.msec.2014.10.051
37. Islam MT, Rodríguez-Hornedo N, Ciotti S, Ackermann C. Rheological characterization of topical carbomer gels neutralized to different pH. Pharm Res 2004; 21: 1192-9. doi:10.1023/b:pham.0000033006.11619.07
38. Çağlar EŞ, Güven GK, Üstündağ Okur N. Preparation and characterization of carbopol-based hydrogels containing dexpanthenol. J Fac Pharm Ankara 2023; 47: 770-83. doi:10.33483/jfpau.1195397
39. de Oliveira ÉL, Ferreira SB, de Castro-Hoshino LV, da Silva Souza Campanholi K, Calori IR, de Morais FA, et al. Thermoresponsive hydrogel-loading aluminum chloride phthalocyanine as a drug release platform for topical administration in photodynamic therapy. Langmuir 2021; 37: 3202-13. doi:10.1021/acs.langmuir.1c00148
40. Trovati G, Sanches EA, Neto SC, Mascarenhas YP, Chierice GO. Characterization of polyurethane resins by FTIR, TGA, and XRD. J Appl Polym Sci 2010; 115: 263-8. doi:10.1002/app.31096
41. Fredi G, Kianfar P, Dalle Vacche S, Pegoretti A, Vitale A. Electrospun shape-stabilized phase change materials based on photo-crosslinked polyethylene oxide. Polymers (Basel) 2021; 13: 2979. doi:10.3390/polym13172979
42. Kianfar P, Vitale A, Dalle Vacche S, Bongiovanni R. Enhancing properties and water resistance of PEO-based electrospun nanofibrous membranes by photo-crosslinking. J Mater Sci 2021; 56: 1879-96. doi:10.1007/s10853-020-05346-3
43. Muyonga JH, Cole CG, Duodu KG. Fourier transform infrared (FTIR) spectroscopic study of acid soluble collagen and gelatin from skins and bones of young and adult Nile perch (*Lates niloticus*). Food Chem 2004; 86: 325-32. doi:10.1016/j.foodchem.2003.09.038
44. Islam MT, Rodréguez-Hornedo N, Ciotti S, Ackermann C. Fourier transform infrared spectroscopy for the analysis of neutralizer-carbomer and surfactant-carbomer interactions in aqueous, hydroalcoholic, and anhydrous gel formulations. AAPS J 2004; 6: e35. doi:10.1208/aapsj060435
45. Sakthiguru N, Sithique MA. Fabrication of bioinspired chitosan/gelatin/allantoin biocomposite film for wound dressing application. Int J Biol Macromol 2020; 152: 873-83. doi:10.1016/j.ijbiomac.2020.02.289
46. Coates J. Interpretation of infrared spectra, a practical approach. In: Meyers RA, ed. Encyclopedia of Analytical Chemistry. Chichester: John Wiley & Sons Ltd; 2000. p. 10815-37.
47. Liu Q, Wu J, Tan T, Zhang L, Chen D, Tian W. Preparation, properties and cytotoxicity evaluation of a biodegradable polyester elastomer composite. Polym Degrad Stab 2009; 94: 1427-35. doi:10.1016/j.polymdegradstab.2009.05.023
48. Frykberg RG, Banks J. Challenges in the treatment of chronic wounds. Adv Wound Care (New Rochelle) 2015; 4: 560-82. doi:10.1089/wound.2015.0635
49. Norouzi M, Moghadasi Boroujeni S, Omidvarkordshouli N, Soleimani M. Advances in skin regeneration: application of electrospun scaffolds. Adv Healthc Mater 2015; 4: 1114-33. doi:10.1002/adhm.201500001
50. Chen S, Liu B, Carlson MA, Gombart AF, Reilly DA, Xie J. Recent advances in electrospun nanofibers for wound healing. Nanomedicine (Lond) 2017; 12: 1335-52. doi:10.2217/nnm-2017-0017
51. Hosseinzadeh S, Soleimani M, Vossoughi M, Ranjbarvan P, Hamedi S, Zamanlui S, et al. Study of epithelial differentiation and protein expression of keratinocyte-mesenchyme stem cell co-cultivation on electrospun nylon/B. vulgaris extract composite scaffold. Mater Sci Eng C Mater Biol Appl 2017; 75: 653-62. doi:10.1016/j.msec.2017.02.101
52. Johnson NR, Wang Y. Drug delivery systems for wound healing. Curr Pharm Biotechnol 2015; 16: 621-9. doi:10.2174/1389201016666150206113720
53. Haider A, Haider S, Kang IK. A comprehensive review summarizing the effect of electrospinning parameters and potential applications of nanofibers in biomedical and biotechnology. Arab J Chem 2018; 11: 1165-88. doi:10.1016/j.arabjc.2015.11.015
54. Niknejad H, Peirovi H, Jorjani M, Ahmadiani A, Ghanavi J, Seifalian AM. Properties of the amniotic membrane for potential use in tissue engineering. Eur Cell Mater 2008; 15: 88-99. doi:10.22203/ecm.v015a07
55. Zong X, Kim K, Fang D, Ran S, Hsiao BS, Chu B. Structure and process relationship of electrospun bioabsorbable nanofiber membranes. Polymer 2002; 43: 4403-12. doi:10.1016/s0032-3861(02)00275-6
56. Joodaki H, Panzer MB. Skin mechanical properties and modeling: a review. Proc Inst Mech Eng H 2018; 232: 323-43. doi:10.1177/0954411918759801
57. Ingraldi AL, Allen T, Tinghitella JN, Merritt WC, Becker T, Tabor AJ. Characterization of amnion-derived membrane for clinical wound applications. Bioengineering (Basel) 2024; 11: 953. doi:10.3390/bioengineering11100953
58. Yao CH, Lee CY, Huang CH, Chen YS, Chen KY. Novel bilayer wound dressing based on electrospun gelatin/keratin nanofibrous mats for skin wound repair. Mater Sci Eng C Mater Biol Appl 2017; 79: 533-40. doi:10.1016/j.msec.2017.05.076
59. Çakmen AB, Noma SA, Gürses C, Köytepe S, Ateş B, Yılmaz İ. Fabrication and characterization of high molecular mass TMPE-based polyurethane wound dressing materials containing allantoin and gentamicin by electrospinning. Nanofabrication 2023; 8: 1-25.

doi:10.37819/nanofab.8.1787
60. Golchin A, Shams F, Kangari P, Azari A, Hosseinzadeh S. Regenerative medicine: injectable cell-based therapeutics and approved products. Adv Exp Med Biol 2020; 1237: 75-95. doi:10.1007/5584_2019_412
61. Yaşayan G, Karaca G, Akgüner ZP, Bal Öztürk A. Chitosan/collagen composite films as wound dressings encapsulating allantoin and lidocaine hydrochloride. Int J Polym Mater Polym Biomater 2021; 70: 623-35. doi:10.1080/00914037.2020.1740993
62. Koob TJ, Lim JJ, Massee M, Zabek N, Denozière G. Properties of dehydrated human amnion/chorion composite grafts: implications for wound repair and soft tissue regeneration. J Biomed Mater Res B Appl Biomater 2014; 102: 1353-62. doi:10.1002/jbm.b.33141
63. Ranjbarvan P, Mahmoudifard M, Kehtari M, Babaie A, Hamedi S, Mirzaei S, et al. Natural compounds for skin tissue engineering by electrospinning of nylon-*Beta vulgaris*. ASAIO J 2018; 64: 261-9. doi:10.1097/mat.0000000000000611
64. Venugopal J, Ramakrishna S. Biocompatible nanofiber matrices for the engineering of a dermal substitute for skin regeneration. Tissue Eng 2005; 11: 847-54. doi:10.1089/ten.2005.11.847
65. Ruiz PA, Jarai G. Discoidin domain receptors regulate the migration of primary human lung fibroblasts through collagen matrices. Fibrogenesis Tissue Repair 2012; 5: 3. doi:10.1186/1755-1536-5-3
66. Olaso E, Labrador JP, Wang L, Ikeda K, Eng FJ, Klein R, et al. Discoidin domain receptor 2 regulates fibroblast proliferation and migration through the extracellular matrix in association with transcriptional activation of matrix metalloproteinase-2. J Biol Chem 2002; 277: 3606-13. doi:10.1074/jbc.M107571200
67. Shams F, Moravvej H, Hosseinzadeh S, Mostafavi E, Bayat H, Kazemi B, et al. Overexpression of VEGF in dermal fibroblast cells accelerates the angiogenesis and wound healing function: in vitro and in vivo studies. Sci Rep 2022; 12: 18529. doi:10.1038/s41598-022-23304-8
68. Chen Y, Yin W, Liu Z, Lu G, Zhang X, Yang J, et al. Exosomes derived from fibroblasts enhance skin wound angiogenesis by regulating HIF-1α/VEGF/VEGFR pathway. Burns Trauma 2025; 13: tkae071. doi:10.1093/burnst/tkae071
69. Landén NX, Li D, Ståhle M. Transition from inflammation to proliferation: a critical step during wound healing. Cell Mol Life Sci 2016; 73: 3861-85. doi:10.1007/s00018-016-2268-0
70. Koob TJ, Rennert R, Zabek N, Massee M, Lim JJ, Temenoff JS, et al. Biological properties of dehydrated human amnion/chorion composite graft: implications for chronic wound healing. Int Wound J 2013; 10: 493-500. doi:10.1111/iwj.12140
71. Galiano RD, Tepper OM, Pelo CR, Bhatt KA, Callaghan M, Bastidas N, et al. Topical vascular endothelial growth factor accelerates diabetic wound healing through increased angiogenesis and by mobilizing and recruiting bone marrow-derived cells. Am J Pathol 2004; 164: 1935-47. doi:10.1016/s0002-9440(10)63754-6
72. Valle KZ, Saucedo Acuña RA, Ríos Arana JV, Lobo N, Rodriguez C, Cuevas-Gonzalez JC, et al. Natural film based on pectin and allantoin for wound healing: obtaining, characterization, and rat model. Biomed Res Int 2020; 2020: 6897497. doi:10.1155/2020/6897497
73. Gurtner GC, Werner S, Barrandon Y, Longaker MT. Wound repair and regeneration. Nature 2008; 453: 314-21. doi:10.1038/nature07039